PRediction Of Geospace Radiation Environment and Solar wind parameterS

Work Package 5
Low energy electrons model improvements to develop forecasting products

Deliverable D5.3
The VERB-IMPTAM low energy seed population

N. Ganushkina, Y. Shprits, A. Castillo, S. Dubyagin
October 30th, 2018

This project has received funding from the *European Union's Horizon 2020 research and innovation programs* under grant agreement No 637302.

Document Change Record

Issue	Date	Author	Details
1.0	21.01.2018	A. Castillo	Initial draft
2.0	25.01.2018	N. Ganushkina	Summary, Sections 2.1 and 4.1, Chapter 7
3.0	16.10.2018	A. Castillo	Chapter 8
4.0	24.10.2018	N. Ganushkina	Partially addressed reviewer comments
5.0	30.10.2018	A. Castillo	Final revised draft

Contents

1 Introduction **5**

2 Model Description **8**
2.1 Model of Ring current electrons from IMPTAM . . . 8
2.2 Simulation of the Radiation Belts with VERB code . . . 10

3 March 17th, 2013 storm **17**
3.1 Electron flux evolution, satellite data . . . 18

4 IMPTAM data **20**
4.1 Results of IMPTAM simulation . . . 20
4.2 Preparation of boundary conditions . . . 25

5 Coupled Simulation **29**
5.1 Stand-alone VERB simulation . . . 29
5.2 Low-Energy Boundary . . . 32
5.3 Upper L^* Boundary . . . 35

6 Conclusions **39**

7 Future tasks and connection to other WPs **41**

8 Update: Model Improvement **42**
8.1 Improvement of the boundary conditions . . . 42
8.2 Improvement of the VERB-IMPTAM coupled model . . . 44
8.3 Final remarks . . . 44

Bibliography **47**

Summary

The Deliverable D5.3 entitled "The VERB-IMPTAM low energy seed population" is the third Deliverable of the Work Package 5 (WP5) "Low energy electrons model improvements to develop forecasting products". The third objective of this WP is to provide the low energy seed population to the VERB radiation belts model. During the work under the Deliverable D5.3, the main focus was set at the Task 5.3 "Providing the low energy seed population to the VERB radiation belts model".

The distribution of low energy electrons, the seed population (10 to few hundreds of keV), is critically important for radiation belt dynamics. This seed population is further accelerated to MeV energies by various processes. All radiation belt models must have a flux defined at a low energy boundary at all L shells. Quite often, the boundary energy is fixed to be several keV. However, the electron flux at these energies varies significantly with geomagnetic activity. It is largely determined by convective and inductive electric fields and varies significantly with substorm activity driven by the solar wind. Satellite measurements cannot provide continuous measurements at 10 to a few hundreds of keV at all MLT and L-shells. Therefore, there is a need in a model which can output the distributions of keV electrons everywhere in the inner magnetosphere. With the development of the Inner Magnetosphere Particle Transport and Acceleration model (IMPTAM) (Ganushkina et al., 2013, 2014), the computational view on the keV electrons is now feasible.

As a part of the work for the Deliverable D5.3, the maps in (L, MLT, pitch angle, energy) of low energy electrons were constructed as output from the improved IMPTAM. The low energy electron maps for the modelled events were be provided to the VERB code as seed keV population for further accelerations to MeV energies. VERB code utilized the seed population for further verification. The coupled VERB with IMPTAM was validated against observations in the heart of the outer radiation belts.

The modeling results are presented for one example storm event on March 15 - 20, 2013. Data of low energy electron fluxes from several satellites in the inner magnetosphere were available for this storm period. For IMPTAM validation, we primarily used the electron fluxes with energies from 5 to 50 keV for our analysis. These energies are most important for surface charging. We focused on the results for AMC 12 measurements at geostationary orbit. The data from the Van Allen Probes inside geostationary orbit were used for the comparisons with the coupled VERB-IMPTAM. AMC12 CEASE electrostatic analyzer measured low energy electron fluxes in 10 channels, covering the range $5-50$ keV. The Van Allen Probes mission consists of two spacecraft in near-equatorial elliptical orbits around Earth, traversing the inner magnetosphere at distances from 1.1 RE to 5.8 RE at a 9-hour period. The two satellites have slightly different orbits, with one lapping the other every 2.5 months. On board of the Van Allen probes, the MagEis instrument measures pitch angle distribution and electron fluxes over the energy range from 30 keV to 4 MeV. The Magnetospheric Electron Detector (MagED) telescope and the Energetic Proton, Electron and Alpha Detector (EPEAD) on board of both GOES satellites also

measure electron fluxes and their pitch angle distributions at energies from about 30 to 600 keV and 0.8 to 2 MeV, respectively, for radial distances close to geostationary orbit (about $L = 6.2$ to 6.8) (Hanser, 2011; Rodriguez, 2014).

Our initial coupled simulations show satisfactory results. The VERB-IMPTAM coupled model is able to reproduce general increases and shape of storm time electron fluxes. The main features of the modeled storm are well observed in our simulations, making the coupled model a suitable forecasting tool. However, overestimation of particle injections indicates possible missing loss mechanisms, that could balance enhanced inward radial diffusion. Improvement of the coupled VERB-IMPTAM model can be performed by including particle losses to the magnetopause and also extending the energy range of IMPTAM simulations to up some 100s of keV, in order to better estimate the behaviour of the electron fluxes at the outer radial boundary.

1 Introduction

Charged particles in the near-Earth space environment are trapped by the Earth's magnetic field forming a the two-zone structure known as the radiation belts or Van Allen belts (Van Allen, 1959). This formation consists of two-ring shaped structures separated by a gap, called the slot region (Van Allen and Frank, 1959; Vernov and Chudakov, 1960; Russell and Thorne, 1970). While the inner electron belt (located below 2 Earth radii) shows rather stable behaviour, the outer belt (located above approx. 3 Earth radii) is strongly dynamic (Rothwell and McIlwain, 1960; Craven, 1966) depending on geomagnetic activity. High-energetic electrons (from 100s of keV to a few MeV) trapped in the Van Allen belts can produce surface or deep dielectric charging on spacecraft materials and damage their electronics (Baker et al., 1996). Strong geomagnetic storms enhance the risk of such operational failures on satellites at all orbits, specially those located in the radiation zones (Lanzerotti, 2001; Odenwald et al., 2006). For these reasons and considering the increasing dependence of our modern society on satellites, studying and understanding the Van Allen belts has become a highly important matter.

The Earth's magnetosphere can be divided into two dynamic regions at the equatorial plane: 1) the diffusion region and 2) the convective region. The diffusion region occupies the area between $L^* = 1$ to almost $L^* = 7$. Here, diffusion is the dominant transport mechanism for electrons. Around $L^* = 7$ a transition zone is observed, and the convective region is found at $L^* > 7$. As inferred form its name, the convective region is characterized by convection as the dominant transport mechanism of electrons. $E \times B$ magnetospheric drift guides particle motion in this region, which, following the conservation of the first adiabatic invariant (μ), will lead particles to gain energy as they move towards the Earth. Due to the influence of the curvature drift and, the charge and energy gradient, electrons will be directed towards the East into the ring current. Low energy electrons are lost to the magnetopause on the day side, but high energy electrons will get trapped by the geomagnetic field and will move along closed field lines around the Earth (Subbotin et al., 2011a).

In particular, the particle population of the radiation belts undergoes a series of acceleration and loss processes occurring in various regions of the magnetospheric environment (Reeves et al., 2003; Millan and Baker, 2012; Turner et al., 2014; Shprits et al., 2008a,b). On one side, the particles in the magnetotail are transported towards the Earth into the plasma sheet by means of magnetospheric convection, where they can be energized to energies of up to 100s of keV (Lyons, 1984). Once these particles convect into the radiation belts (Baker and Stone, 1978; Elkington et al., 2004) , their interaction with a variety of plasma waves (e.g. ULF, VLF, ELF waves) will determine the course of their dynamics (Jacobs et al., 1964). For example, it has been reported in the past (Reeves et al., 1998), that low energy particles (in the range of 10s of keV) undergoing radial transport and local acceleration are accelerated within the radiation belts. This dynamic effect generates peaks in phase space density (or electron flux) around $L^* = 4 - 5$. For this reason, the role of the low energy seed population in the dynamics of the radiation belts has a high importance.

In quasi-linear theory, it is possible to describe non-adiabatic processes in terms of radial, energy and pitch angle diffusion, under the assumption that collisionless charged particles in the ambient magnetic field experience resonant interactions with incoherent electromagnetic waves that have rather small amplitudes (Kennel and Engelmann, 1966; Lerche, 1968; Schulz and Lanzerotti, 1974; Drozdov et al., 2015). The resulting mathematical law is called the Fokker-Planck diffusion equation, which delivers the variation of Phase Space Density (PSD) in adiabatic invariant coordinates (Green and Kivelson, 2001; Shprits et al., 2008a). Using a high plasma density approximation, simplified initial diffusion rates needed to solve the equation were estimated (Lyons et al., 1971). This initial approach allowed the evaluation of losses due to whistler mode plasmaspheric hiss waves (Lyons et al., 1972) and provided an explanation for the two zone structure of Earth's radiation belts (Lyons and Thorne, 1973). Several studies have presented alternative methods for the calculation of quasi-linear diffusion rates (Glauert and Horne, 2005; Albert and Young, 2005; Albert, 2007; Ni et al., 2008; Shprits and Ni, 2009).

The first computational solution of the 3-D Fokker-Planck equation was the Salammbô code (Beutier and Boscher, 1995; Bourdarie et al., 1996, 1997; Boscher et al., 2000), which was able to perform simulations including radial diffusion driven by electrostatic and magnetic field fluctuations, cosmic ray albedo decay, losses due to plasmaspheric hiss, and Coulomb collisions. Simulations accounting for diffusion due to chorus waves showed that MeV electrons can efficiently be scattered and accelerated during resonant wave-particle interactions in the radiation belts (Varotsou et al., 2005; Horne et al., 2005), and that the interplay of radial diffusion and local acceleration can lead to the acceleration of keV electrons to MeV energies in the outer belt (Varotsou et al., 2008; Shprits et al., 2009b). Initial simulations also helped to recognize the importance of increased particle losses due to outward radial diffusion, as reported in numerous studies (Brautigam and Albert, 2000; Miyoshi et al., 2003, 2006). Also, depletion of energetic fluxes observed at different energies for certain geomagnetic events, indicated the fundamental role of magnetopause losses and convective sources in the dynamics of the radiation belts (Shprits et al., 2006). Interaction of MeV electrons with EMIC and hiss waves in plumes produces rapid particle losses (Li et al., 2007). The solution of the 3-D Fokker-Planck equation, that includes radial diffusion due to ULF waves, and energy, pitch angle, and mixed energy–pitch angle diffusion due to chorus waves, suggests that the mixed diffusion term is only important for electrons with equatorial pitch angles not larger than 30° (Albert et al., 2009; Subbotin et al., 2010; Xiao et al., 2010). Simulations accounting for magnetospheric convection have shown the dominance of this mechanism in the injection of the low-energy electron seed population and the importance of radial diffusion for the transport of high energy particles to lower L shells (Jordanova and Miyoshi, 2005).

The electron seed population can be obtained from observations near geosynchronous orbit. However, for the purpose of real-time forecasting and to understand the underlying physical processes, numerical models should be used to obtain evolution of fluxes at these energies. Such models are important to describe the dynamics of low energy particles. In the current study, we describe initial simulations computed with the coupled model of the VERB code (Subbotin and Shprits, 2009; Shprits et al., 2009b) and the Inner Magnetospheric Particle Transport and Acceleration Model (IMPTAM) (Ganushkina et al., 2005, 2006, 2012). In this study, one-way code coupling has been used, with the electron fluxes computed by IMPTAM being input into the VERB code. The numerical models, wave models, boundary and initial conditions underlying the VERB and IMPTAM codes are explained in Chapter 2. The geomagnetic event chosen to test and validate the coupled model is presented in Chapter 3. The results of the IMPTAM simulation that serve to generate the boundary conditions for VERB are described in Chapter 4, together with the data processing performed on these results, in order to make them suitable for the coupling process. Chapter 5 contains the results of two initial coupled simulations and the summary of this study is given in Chapter 6.

2 Model Description

The theoretical background of the IMPTAM and VERB codes, as well as the set up used to perform the initial coupled simulations are described in the following sections.

2.1 Model of Ring current electrons from IMPTAM

The IMPTAM (Ganushkina et al., 2013, 2014, 2015) traces distributions of electrons in the drift approximation with arbitrary pitch angles from the plasma sheet to the inner L-shell regions with energies reaching up to hundreds of keVs in time-dependent magnetic and electric fields. We trace a distribution of particles in the drift approximation, and we take into account the $E \times B$ drift, and magnetic drifts with bounce-averaged drift velocities. Relativistic effects for electrons are taken into account in the drift velocities.

To follow the evolution of the particle distribution function f and particle fluxes in the inner magnetosphere dependent on the position R, time t, energy E_{kin}, and pitch angle α, it is necessary to specify: (1) particle distribution at initial time at the model boundary; (2) magnetic and electric fields everywhere dependent on time; (3) drift velocities; (4) all sources and losses of particles. The changes in the distribution function $f(R, \varphi, t, E_{kin}, \alpha)$, where R and φ are the radial and azimuthal coordinates in the equatorial plane, respectively, are obtained by solving the equation:

$$\frac{\partial f}{\partial t} = \frac{\partial f}{\partial t} V_\varphi + \frac{\partial f}{\partial t} V_R + \text{sources} - \text{losses}, \tag{1}$$

where V_φ and V_R are the azimuthal and radial components of the bounce-averaged drift velocity. The model boundary can be set in the plasma sheet at distances, depending on the scientific questions we are trying to answer, from $6,6\ R_E$ to $10\ R_E$. Liouville's theorem is used to gain information of the entire distribution function by mapping the boundary conditions throughout the simulation domain, including loss process attenuation, through the time-varying magnetic and electric fields.

For the obtained distribution, we apply radial diffusion which plays a significant role in electron energization. We solve the radial diffusion equation (Schulz and Lanzerotti, 1974) for the obtained distribution function. Kp-dependent radial diffusion coefficients D_{LL} for the magnetic field fluctuations are computed following Brautigam and Albert (2000). Since diffusion by the magnetic field fluctuations at $L > 3$ dominates diffusion produced by electrostatic field fluctuations (Shprits and Thorne, 2004), we ignore the electrostatic component of the radial diffusion coefficient. At the next time step we repeat the order of calculation: first we solve transport with losses and then apply the diffusion.

Convective outflow, Coulomb collisions and loss to the atmosphere are taken into account. We assume strong pitch angle scattering at the distances where the ratio between the radius of the field line curvature in the equatorial current sheet (R_c) and the effective

Larmor radius ρ varies between 6 and 10 (Sergeev and Tsyganenko, 1982; Büchner and Zelenyi, 1987; Delcourt et al., 1996). Electron precipitation to the atmosphere is calculated similarly to Jordanova et al. (2008) with a time scale of a quarter bounce period, and the loss cone corresponds to an altitude of 200 km. We take into account pitch angle diffusion due to wave-particle interactions by introducing the parameterizations of the electron lifetimes due to interactions with chorus and hiss waves by Orlova and Shprits (2014) and Orlova et al. (2014, 2016) with the activity-dependent plasmapause location by Carpenter and Anderson (1992).

IMPTAM can utilize any magnetic or electric field model. IMPTAM can take into account the self-consistency of the magnetic field by calculating the magnetic field produced by the model currents and feeding it back to the background magnetic field. At the same time, when using realistic model magnetic field such as Tsyganenko models which contain the prescribed ring and near-Earth tail currents, it is necessary to remove the model currents from the background magnetic field model and consider self-consistent calculations of the magnetic field. Since we study the electrons, their contribution to the ring current is no more than 10%, so their contribution to the distortion of the background magnetic field is small. Taking into account the electric field in a self-consistent way is of high importance when modeling the inner magnetosphere particles (Fok et al., 2003; Liemohn and Brandt, 2005). In our study, we focus on low-energy electrons and, therefore, neglect electron pressures in the total pressure as their effect is small/insignificant, so the chosen field models do not require any modifications for self-consistency effects. In addition to the large-scale fields, transient fields associated with the dipolarization process in the magnetotail during substorm onset were modeled (e.g. Ganushkina et al. 2005) as an earthward propagating electromagnetic pulse of localized radial and longitudinal extent (Li et al., 1998; Sarris et al., 2002).

IMPTAM setup for modeling of keV electrons

IMPTAM is driven by various solar wind, IMF and geomagnetic indices which are used as inputs for the different components of IMPTAM. We used Tsyganenko T96 magnetic field model (Tsyganenko, 1995) which uses the Dst index, P_{SW}, and IMF B_Y and B_Z as input parameters. The electric field was determined using V_{SW}, the IMF strength B_{IMF} and B_Y and B_Z (via IMF clock angle θ_{IMF}) being the Boyle et al. (1997) ionospheric potential Φ mapped to the magnetosphere.

We set the model boundary at 10 R_E and use the kappa electron distribution function. We set $k = 1.5$. Our results presented as part of the review paper by Horne et al. (2013) indicated that decreasing the k parameter from 5 to 1.5 gave the best agreement between the modeled and the observed electron fluxes with $50 - 150$ keV energies at geostationary orbit onboard the LANL satellites. In our model, we assume that the distribution can be fitted by the kappa shape only in the finite range of velocities.

Parameters of the kappa distribution function are the number density N_{ps} and temperature T_{ps} in the plasma sheet given by the Dubyagin et al. (2016) empirical model, constructed at distances between 6 and 11 R_E based on THEMIS data. The N_{ps} is driven by the solar wind number density N_{sw} and southward IMF component B_S. The T_{ps} is dependent on the solar wind velocity V_{sw}, the southward B_S and northward B_N IMF components. Here, B_S and B_N are defined as follows: B_S = -IMF B_Z, if IMF $B_Z < 0$ and $B_S = 0$, if IMF $B_Z \geq 0$; $B_N = 0$, if IMF $B_Z < 0$ and B_N = IMF B_Z, if IMF $B_Z \geq 0$.

Substorm-associated electromagnetic fields are taken into account in IMPTAM (Ganushkina et al., 2013, 2014) in a similar form to the Li et al. (1998) and Sarris et al. (2002) model to represent an earthward-propagating electromagnetic pulse of localized radial and longitudinal extent. The pulse is present during about 10 min. Instead of approximating the front velocity as a linear function as was done by Sarris et al. (2002), we introduce the radial dependence as:

$$v(r) = ar^2 + br + c, \tag{2}$$

where $a[km^{-1}sec^{-1}] = 6.37$, $b[sec^{-1}] = -50.6$, $c[km/sec] = 108$ to match the observed velocity values (Ohtani, 1998; Sergeev et al., 1998; Reeves et al., 1996; Apatenkov et al., 2007, 2009). The model has the ability to automatically adjust the velocity of the pulse depending on where the pulse is initiated and at various speeds as it is expected for the velocity of the pulse to vary with the amplitude of the pulse and indirectly with the magnitude of a substorm. The pulse stops at 3.5 R_E. The magnetic field disturbance from this dipolarization process is obtained from Faraday's law. We launch a pulse at each substorm onset determined from the AE index and scaled the amplitude according the maximum values of the AE.

2.2 Simulation of the Radiation Belts with VERB code

The modified Fokker-Planck equation describes time-changes of the phase-averaged phase space density (PSD or f) in the magnetosphere of the Earth, in terms of the three adiabatic invariants (Schulz and Lanzerotti, 1974; Walt, 1994):

$$\frac{\partial f}{\partial t} = \sum_{i,j=1}^{3} \frac{\partial}{\partial I_i} D_{I_i I_j} \frac{\partial f}{\partial I_j} \tag{3}$$

where $I_1 = \mu, I_2 = J, I_3 = \Phi$ are the three adiabatic invariants and $D_{I_i I_j}$ are the diffusion coefficients. The adiabatic invariants can be expressed as:

$$\begin{aligned} \mu &= \frac{p_\perp^2}{2m_0 B}, \\ J &= \int_{bounce} p_\parallel \, ds, \\ \Phi &= \oint_{drift} B \, dS. \end{aligned} \tag{4}$$

Using bounce and drift averaged diffusion coefficients ($D_{L^*L^*}$, D_{pp}, $D_{p\alpha_0}$, $D_{\alpha_0 p}$, $D_{\alpha_0\alpha_0}$), equation (3) can be transformed into (L^*, p, α_0) coordinates and is known as the bounce-averaged Fokker-Planck-equation:

$$\frac{\partial f}{\partial t} = {L^*}^2 \frac{\partial}{\partial L^*}\bigg|_{\mu,J} \left(\frac{1}{{L^*}^2} D_{L^*L^*} \frac{\partial f}{\partial L^*}\bigg|_{\mu,J} \right) + \frac{1}{p^2}\frac{\partial}{\partial p}\bigg|_{\alpha_0,L^*} p^2 \left(D_{pp} \frac{\partial f}{\partial p}\bigg|_{\alpha_0,L^*} + D_{p\alpha_0} \frac{\partial f}{\partial \alpha_0}\bigg|_{p,L^*} \right) + \\ \frac{1}{T(\alpha_0)\mathrm{sin}(2\alpha_0)} \frac{\partial}{\partial \alpha_0}\bigg|_{p,L^*} T(\alpha_0)\mathrm{sin}(2\alpha_0) \left(D_{\alpha_0\alpha_0} \frac{\partial f}{\partial \alpha_0}\bigg|_{p,L^*} + D_{\alpha_0 p} \frac{\partial f}{\partial p}\bigg|_{\alpha_0,L^*} \right) - \frac{f}{\tau_{/c}}, \tag{5}$$

where α_0 is the equatorial pitch angle, p is the relativistic momentum and L^* is a measure related to the radial distance L and is defined as $L^* = (2\pi M)/(\Phi R_E)$, where $M = 8.07 \times 10^22$ Am^2 represents the magnetic moment of the Earth's dipole field and $R_E = 6371km$ is the Earth radius. $T(\alpha_0)$ is an approximation of the bounce frequency in a dipole field and was estimated after Lenchek et al. (1961) as:

$$T(\alpha_0) = 1.3802 - 0.3198 \left(\mathrm{sin}\alpha_0 + \mathrm{sin}^{1/2}\alpha_0 \right) \tag{6}$$

Non-adiabatic particle motion caused, for example, by rapid electromagnetic fluctuations can corrupt conservation of some adiabatic invariants and lead to transport by diffusion. In equation (3) the radial diffusion of particles in terms of PSD is described by the first term on the right hand side, where $D_{L^*L^*}$ is the radial diffusion coefficient. In contrast to the other terms of the equation, the radial diffusion term is written in terms of L^*, μ, J, which are necessary as radial diffusion leads to particle transport along constant μ and J, but does not conserve L^* (Schulz and Lanzerotti, 1974). Also, adiabatic motion of particles due to slow variations in the magnetic field configuration occurs under conservation of all three adiabatic invariants and can be accounted for by using these phase space coordinates.

The second, third and fourth terms of equation (3) describe local processes. Momentum diffusion with diffusion coefficient D_{pp} is given by the second term. Since the relativistic momentum is related to energy by $E = \sqrt{p^2c^2 + m^2c^4} - mc^2$ (where m is the rest mass of the electron ($m = 9,11 \times 10^{-31}$ kg), and c is the speed of light in vacuum ($c = 2.998 \times 10^8$ m s^{-1}), the momentum diffusion is commonly also known as "energy diffusion". The pitch angle diffusion process is described by the third term, where $D_{\alpha_0\alpha_0}$ is the diffusion coefficient, and the fourth term estimates dynamics due to mixed diffusion, where $D_{p\alpha_0} = D_{\alpha_0 p}$ is the corresponding diffusion coefficient.

The last term on the right hand side of equation (3), $(f/\tau_{/c})$, accounts for the losses inside the loss cone. Here, $\tau_{/c}$ is a characteristic lifetime assumed to be infinite for particles with pitch angles outside the loss cone and otherwise, equal to 1/4 of a bounce period. In this study, cross L-pitch angle diffusion was not taken into account (O'Brien, 2014).

Diffusion Coefficients

In order to solve equation (3) numerically, all four diffusion coefficients must be estimated. Since radial diffusion is product of resonant wave-particle interactions with ULF-waves in the Pc4 to Pc5 range (i.e. $7 - 22$ mHz and $2 - 7$ mHz, respectively), both magnetic and electric components of the ULF-waves should be taken into account for the calculation of the radial diffusion coefficient ($D_{L^*L^*}$). The magnetic component used by the VERB-code is taken from Brautigam and Albert (2000):

$$D_{L^*L^*} = 10^{0.056K_p - 9.325} {L^*}^{10} \tag{7}$$

and used for all Kp values. Electric field variations appear to have a reduced influence on radial diffusion dynamics of the particles in the radiation belts (Brautigam and Albert, 2000). The electric component of the radial diffusion coefficient is therefore assumed to be negligible in our simulations.

For a simplified computation of the local scattering rates, dipole geometry is adopted in this study. Table 2.1 presents an overview of the applied wave model, for the estimation of the resting diffusion coefficients. Day and night side chorus wave parametrizations are taken from e.g. Shprits et al. (2009b). Chorus waves generate diffusion outside the plasmasphere. However, waves in the day or night sector have different effects on particle dynamics, because of their differential latitudinal distribution. Day side chorus waves scatter electrons in the outer radiation belt into the loss cone causing rapid particle losses, while night side chorus is mostly responsible for the acceleration of particles observed during the recovery phase of geomagnetic storms (Li et al., 2007). The diffusion coefficients of chorus species were computed by the Full Diffusion Code (FDC) (Ni et al., 2008; Shprits and Ni, 2009) for absolute resonance orders of up to five ($n \leq |5|$) and for $Kp = 4$.

Hiss waves, lightning-generated whistler waves and VLF waves of anthropogenic origin produce particle losses inside the plasmasphere (Subbotin et al., 2011b). For the parametrization of plasmasheric hiss, parameters from Orlova et al. (2014) were used. This model is based on quadratic fits to the hiss amplitudes on day and night side, as a function of L-shell, Kp and latitude. The fits were estimated using data from the CRRES wave experiment, considering the increase of obliquity of hiss waves as these propagate along the field line (Agapitov et al., 2013; Thorne et al., 2013). Similar to previous studies, the frequency spectrum of hiss waves is taken as Gaussian. Wave parameters for lightning-generated waves are calculated according to Meredith et al. (2007), while parameters for anthropogenic VLF waves are based on Abel and Thorne (1998); Starks et al. (2008). Diffusion rates estimated for chorus, hiss and lightning-generated whistler waves

Wave type	$B_w(pT)$	λ_{max}	*Density model*	*Percent MLT*	*Wave spectral properties*	*Distribution in wave normal*
Chorus day	$10^{0.75+0.04\lambda}(2 \times 10^{0.73+0.91Kp})^{0.5}/57.6$ for $Kp \leq 2+$; $10^{0.75+0.04\lambda}(2 \times 10^{2.5+0.18Kp})^{0.5}/57.6$ for $2+ < Kp \leq 6$	35	Sheeley et al. (2001)	25%	$\omega_m/\Omega_e = 0.2$, $\delta\omega/\Omega_e = 0.1$, $\omega_{uc}/\Omega_e = 0.3$, $\omega_l c/\Omega_e = 0.1$.	$\theta_m = 0°$, $\delta\theta = 30°$, $\theta_{uc} = 45°$, $\theta_{lc} = 0°$
Chorus night	$50(2 \times 10^{0.73+0.91Kp})^{0.5}/57.6$ for $Kp \leq 2+$; $50(2 \times 10^{2.5+0.18Kp})^{0.5}/57.6$ for $2+ < Kp \leq 6$	15	Sheeley et al. (2001)	25%	$\omega_m/\Omega_e = 0.35$, $\delta\omega/\Omega_e = 0.15$, $\omega_{uc}/\Omega_e = 0.65$, $\omega_{lc}/\Omega_e = 0.65$.	$\theta_m = 0°$, $\delta\theta = 30°$, $\theta_{uc} = 45°$, $\theta_{lc} = 0°$
Lightning generated whistlers	3	45	Carpenter and Anderson (1992)	100%	$f_m = 2000$ Hz, $\delta f = 4500$ Hz, $f_{uc} = 6500$ Hz, $f_{lc} = 2500$ Hz	$\theta_m = 45°$, $\delta\theta = 22.5°$, $\theta_{uc} = 22.5°$, $\theta_{lc} = 67.5°$
Anthropogenic 1	0.8	45	Carpenter and Anderson (1992)	$4 \times 2.4\%$	$f_m = 17100$ Hz, $\delta f = 50$ Hz, $f_{uc} = 17000$ Hz, $f_{lc} = 17200$ Hz	$\theta_m = 45°$, $\delta\theta = 22.5°$, $\theta_{uc} = 22.5°$, $\theta_{lc} = 67.5°$
Anthropogenic 2	0.8	45	Carpenter and Anderson (1992)	$4 \times 2.4\%$	$f_m = 22300$ Hz, $\delta f = 50$ Hz, $f_{uc} = 22400$ Hz, $f_{lc} = 22200$ Hz	$\theta_m = 45°$, $\delta\theta = 22.5°$, $\theta_{uc} = 22.5°$, $\theta_{lc} = 67.5°$

Table 2.1: Wave parameters used for the computation of the diffusion coefficients. In the chorus model, the wave frequency distribution (given in angular frequency ω, [rad/s]) is assumed Gaussian with maximum ω_m, bandwidth $\delta\omega$ and lower and upper cutoffs ω_{lc} and ω_{uc}, respectively. These parameters are proportional to the absolute equatorial gyrofrequency of the electron Ω_e. In the other wave models, the wave frequency distribution is also assumed Gaussian, but defined in temporal frequency (f, [Hz]) being: f_m the maximum, δf the bandwidth, f_{uc} the upper cutoff and f_{lc} the lower cutoff. Similarly, the wave normal angle has a Gaussian distribution with peak at θ_m, bandwidth $\delta\theta$, upper cutoff θ_{uc} and lower cutoff θ_{lc}.

were averaged over magnetic local time (MLT) and scaled throughout the simulation using the Kp-index and the variation of wave power, in order to represent the variation of wave activity during storm-time (Carpenter and Anderson, 1992; Sheeley et al., 2001; Shprits et al., 2007). The chosen plasmaspheric density model is based on Denton et al. (2004, 2006) and the plasmapause position is calculated after Carpenter and Anderson (1992):

$$L_{pp} = 5.6 - 0.46Kp_{max24} \tag{8}$$

where Kp_{max24} is the maximum value of Kp in the previous 24 hours prior to the simulation time (t).

Boundary and Initial Conditions

The VERB-code computes the numerical solution of equation (5) using implicit finite differences on a high resolution grid with 46 × 101 × 91 points for radial, energy and equatorial pitch angle diffusion, respectively (Drozdov et al., 2015). In order to obtain better resolution in high-PSD regions, such as observed for low energy particles and at the edge of the loss cone, logarithmic distribution is used for energy and equatorial pitch angle grid points (Subbotin et al., 2011b). The contribution of radial, local and mixed diffusion processes to the total PSD variation are calculated separately as a single operator for each diffusion type applying the operator-splitting method, which optimizes the computational efficiency of the code (s. Subbotin and Shprits (2009) for more detailed information).

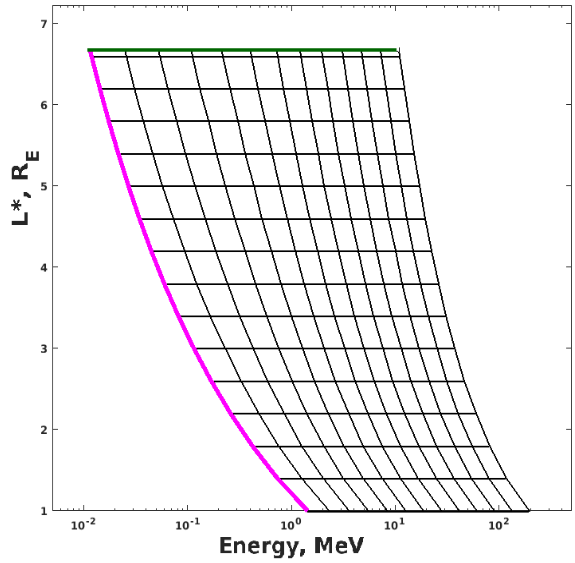

Figure 2.1: 2-D section of the computational grid of the VERB-3D code. Green and magenta lines indicate upper L^* and lower energy boundary conditions, respectively, provided by the IMPTAM code for the VERB simulations.

The bounce-averaged Fokker-Planck equation (Eq. 5) is solved for a range of L^* from 1 to 6.6 and for equatorial pitch angles from 0° to 90°. Selecting $L^* = 6.6$ as the upper boundary of the radial diffusion operator is reasonable, since this is commonly a closed drift shell and physics of radial diffusion apply for particles inside geosynchronous orbit (Subbotin et al., 2011b). In order to estimate the lower energy boundary, we have to take into account that electrons moving earthwards conserve the first and second adiabatic invariants (μ and J, respectively), and undergo energization due to the increasing magnetic field strength (Schulz and Lanzerotti, 1974). Also, the low energy boundary should not be chosen below 10 keV, as the dynamics of particles at lower energies are rather less influenced by diffusion processes (Liu et al., 2003; Horne et al., 2005). Choosing $\mu \approx 10$ MeV/G for the low energy boundary allows to resolve energies around 10 keV at the upper radial boundary ($L^* = 6.6$). Using equation (4), we can estimate the energy of particles with this μ at lower L-shells and define the lower energy boundary for the VERB simulations. Figure 2.1 shows a cross-section of the computational grid used in the VERB-3D code. The lower energy boundary, $\mu \approx 10$ MeV/G, is marked as the magenta line. Lines parallel to the low energy boundary represent different μ values. As observed in Figure 2.1, the VERB grid is irregular in the energy range and energy values increase with decreasing L^* (Subbotin and Shprits, 2009).

Boundary	*Condition*	*Underlying physical processes*
$\alpha_0 = 0°$	$\partial(PSD)/\partial\alpha_0 = 0$	Strong and weak diffusion regimes
$\alpha_0 = 90°$	$\partial(PSD)/\partial\alpha_0 = 0$	Flat pitch angle distribution
$L^* = 1$	$PSD = 0$	Losses to the atmosphere
$L^* = 6.6$	$PSD(time)$	Coupling with IMPTAM
$E = E_{min}$	$PSD(time)$	Coupling with IMPTAM
$E = E_{max}$	$PSD = 0$	Absence of multi-MeV energy electrons

Table 2.2: Boundary conditions used for the VERB-IMPTAM coupled simulations.

For each grid operator two boundary conditions, one upper and one lower PSD value, are needed in order to perform a VERB simulation. Table 2.2 presents a summary of the boundary conditions used in this study. Assumption of a flat pitch angle distribution at the upper pitch angle boundary ($\alpha_0 = 90°$) is described applying here a zero PSD-derivative condition (Horne et al., 2003). Strong and weak diffusion regimes at 0° pitch angle are accounted for, by setting the PSD-derivative at the lower pitch angle boundary equal to zero (Shprits et al., 2009a). Particle losses to the atmosphere are simulated by using PSD equal to zero at $L^* = 1$. At the upper energy boundary, a zero PSD boundary condition is applied, representing the absence of high-energy particles (> 10 MeV) electrons (Subbotin and Shprits, 2009; Subbotin et al., 2011b; Drozdov et al., 2015). Initial PSD values are calculated as the steady state solution of the radial diffusion equation:

$$L^{*2} \frac{\partial}{\partial L^*} \left(\frac{1}{L^{*2}} D_{L^*L^*} \frac{\partial f}{\partial L^*} \right) - \frac{f}{\tau} = 0, \tag{9}$$

where the diffusion coefficient $D_{L^*L^*}$ is estimated for quite times (Kp = 2) and the electron lifetime τ is set equal to three days (Shprits et al., 2005).

The lower energy and upper L^* boundaries show very dynamic variations of PSD during storm times. For this reason, more realistic results of our simulations can be obtained by using time dependent satellite observations or modelled fluxes from other simulation codes. In this study, we incorporate results from the ring current model IMPTAM at the low energy and upper L^* computational boundaries of our simulations with the VERB code. The independence of IMPTAM from observations of the radiation belt environment, is the perfect condition to use the coupled model for prediction purposes. Computation, selection and processing of the boundary data, as well as the description of the coupling process are explained in chapter 4.

3 March 17th, 2013 storm

For the initial coupling of IMPTAM and VERB, we have chosen to study the geomagnetic storm that reached the Earth on March 17th, 2013. This event is well known in the magnetospheric physics community, because is has been the strongest storm in the Van Allen probe period. Therefore, the event has also been chosen by the scientific modeling community (Geospace Environment Modeling (GEM) and Community Coordinated Modeling Center (CCMC)) as a challenging event to reproduce. Many satellite observations for this period of time are available and, in particular, excellent coverage over the entire outer Van Allen belt region is given.

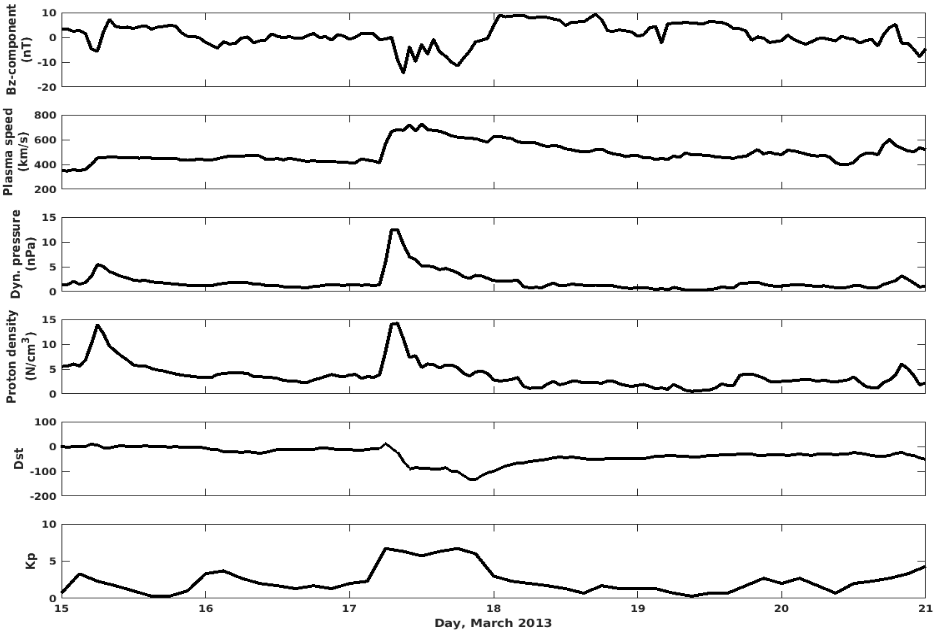

Figure 3.2: Magnetic field and solar wind parameters for the March 17, 2013 strom. From top to bottom: Z-component of the IMF, solar wind velocity, dynamic pressure, number density, Dst and Kp indexes.

Figure 3.2 shows different magnetic field (B) (Fig.3.2, panels 1) and solar wind parameters (Fig.3.2, panels 2,3,4), together with the Dst and the Kp indexes (Fig.3.2, panels 5,6) for the time period 15th to 20 of March, 2013. From the image we recognize two geomagnetic events, that took place during this 6-day period. One during the first half of March 15th (first day) and the second event (the studied event) starting on the early UT hours of the 17th of March. While the first storm appear to have a duration of only a few hours, the second storm lasts almost throughout one entire day.

The event on the 15th of March has a rather minor magnitude as inferred from the north-south component of the interplanetary magnetic field (IMF), which shows a moderate decrease becoming thereby more southward by about (5 nT) (Fig.3.2, panel 1). Plasma velocity also increased by about 100 km/s (Fig.3.2, panel 2), as well as the solar dynamic pressure of the IMF around 5 nPa (Fig.3.2, panel 3). Proton density is also enhanced by about 8 units (Fig.3.2, panel 4). While the Kp-index clearly increases up to

$Kp \approx 4$, Dst shows only minor variation during this event. Although, of minor strength, this storm might have produced abundant electrons population of keV energies that will affect our simulations, increasing fluxes of such particles in the heart of the outer belt.

During the days previous to the main geomagnetic storm, only quiet time variations are observed in the different parameters and indexes. Throughout this period solar plasma parameters that had been enhanced due to the first minor storm, decreased and stabilized. On the day of the storm, a strong southward B_z-component of the IMF (about -15 nT) was measured (Fig.3.2, panel 1). Sudden enhancements of the plasma velocity (by about 300 km/s) (Fig.3.2, panel 2), plasma pressure by over 10 nPa (Fig.3.2, panel 3) and proton density (Fig.3.2, panel 4) are observed. The north-south component of the IMF increases and oscillates for some hours, but in the afternoon time starts decreasing again to down to -10 nT. Dst and Kp indexes (Fig.3.2, panel 5 and 6, respectively) show two maxima peaks during this storm, similar to B_z-component. Right at te beginning of the storm Dst drops to -100 and stays so low for a couple of hours, until its values drop below -140 in the late hours of March 17th. The Kp-index also reaches two maxima at about the same hours as Dst, with values of $Kp \approx 7-8$. Satellite observations available for this time period in relevant regions will be presented in the next section.

3.1 Electron flux evolution, satellite data

One of the advantages of this storm, is the availability of high-quality satellite data in the radiation belt region and throughout the entire storm. Satellite measurements from instruments on board of Van Allen Probes (MagEis, on both probes A and B) together with observations from GOES satellite (MagED telescope, on board of both satellites 13 and 15) provide electron fluxes for energies from 10s of keV up to 4 MeV at $L^* = 2-5.8$ and $L^* = 5-6.6$, respectively, covering the entire radial extent of the outer radiation belt. Figure 3.3 presents electron fluxes measured by MagED telescope and MagEis instrument, for particles at 85° equatorial pitch angle at different energies, in figure 3.3, panels a) 0,06; b) 0,1; c) 0,4; d) 0,9 MeV, respectively. Electrons of different energies show very different flux evolution during the presented period of time.

At 60 keV energy (Fig.3.3.a), fluxes exhibit quiet time levels during the initial hours of the first day. On the second half of the first day (March 15th) fluxes above $L^* = 5$ are enhanced by about one order of magnitude, due to the minor storm taking place at that time. Particles are energized and inward transport is observed during the 16th of March, when the lower boundary of the outer belt moves to lower L^* (around $L^* = 4$). On the 17th, electron fluxes are suddenly increased by up to two orders of magnitude, reaching their maximum values. Around $L^* = 3$ fluxes develop a peak, that is present throughout the recovery phase. Fluxes above $L^* \approx 3.5$ are lower than peak fluxes, but still remain about one order of magnitude higher than pre-storm levels. During the last two days (19th and 20th), slow flux decay can be observed.

Electrons of 100 keV energy (Fig.3.3.b), have quiet time fluxes throughout March 15th (first day). The lower L^* boundary of the outer belt for this energy is located between

$L^* = 4 - 4.5$. On the second half of day 16, electron fluxes are enhanced moderately and the lower L^* boundary of the outer belt moves below 4. The fluxes observed on the day of the storm undergo an abrupt increase of about two orders of magnitude and the lower L^* boundary vanishes below $L^* = 2.5$. From the 17th to 19th, fluxes at all L^* remain considerably high with a diffusion-generated peak around $L^* = 3$. On the 20th, initial flux decay becomes visible above $L^* = 3.5$, where fluxes decrease to moderate magnitudes.

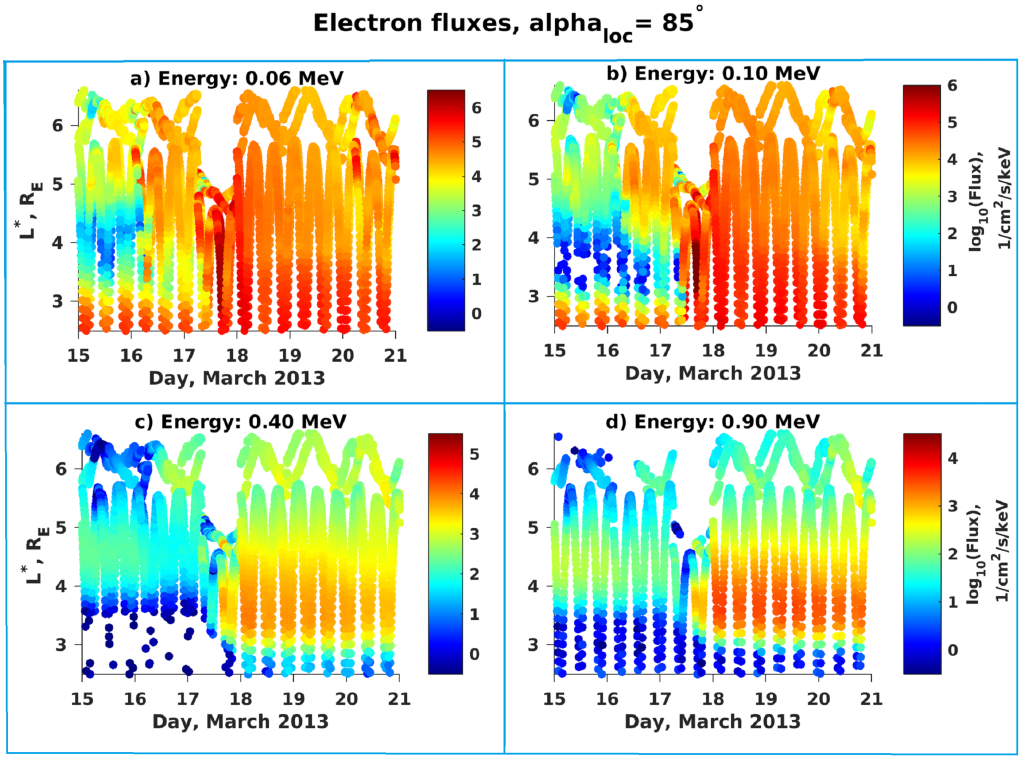

Figure 3.3: Observations from GOES and Van Allen probes as function of L^* and time. Electron fluxes at local pitch angle $\alpha_{loc} = 85°$ for different energies are displayed. Panels: a) 0.06 MeV, b) 0.10 MeV, c) 0.40 MeV and d) 0.90 MeV, respectively. Note: scales are different for each panel. (Data from Omniweb)

Electrons with energies between 400 to 900 keV (Fig.3.3.c,d), behave very different, than particles of lower energies. On the first day, particles of these energies are confined within $L^* = 4$ to 5 and do not appear to be affected by the minor geomagnetic storm. During the second half of day 16, energization of particles at $L^* > 5.5$ is indicated by measurements of the GOES satellites. At the same time, MagEis data shows minor motion of the lower boundary of the belt towards higher L^*, suggesting outward particle transport just prior to the major storm. During the main event, electron fluxes increase by up to two orders of magnitude and the lower L^* boundary moves inwards to $L^* = 3$. The maximum peak is well defined around $L^* = 3.5$. From the second half of March 19th, continuous reduction of fluxes starts taking place. This very characteristic evolution of fluxes and the good quality of the available data make the March 17th storm an adequate event for the testing and validation of our coupled model.

4 IMPTAM data

In this section, we present the results from the simulations performed with the IMPTAM code, which will provide the data for the boundary conditions that are needed to coupled both models.

4.1 Results of IMPTAM simulation

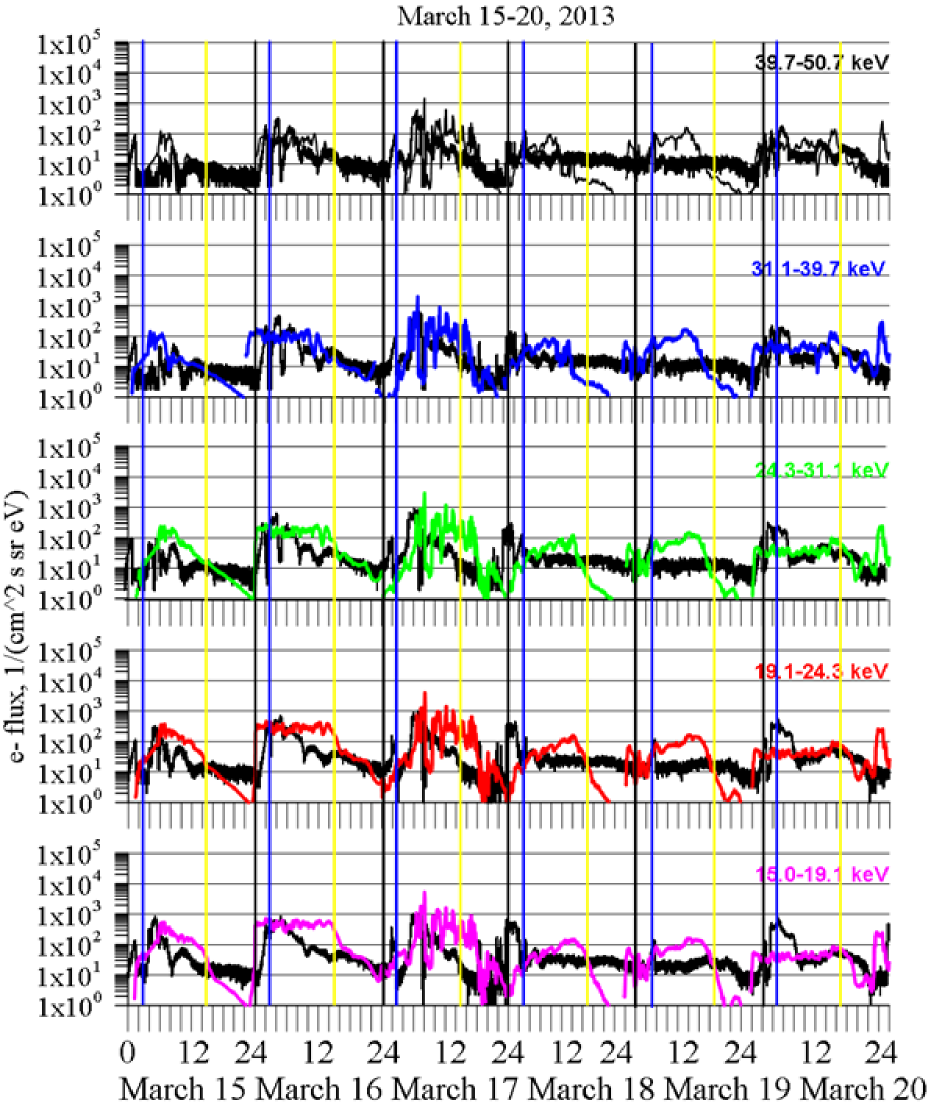

Figure 4.4: Electron fluxes at geostationary orbit measured by the CEASE II ESA instrument onboard the AMC 12 satellite (thin black curves) and modeled with IMPTAM for: first panel 39.7 – 50.7 keV (thin black curve), second panel 31.1 – 39.7 keV (blue curve), third panel 24.3 – 31.1 keV (green curve), forth panel 19.1 – 24.3 keV (red curve), and fifth panel 15.0 – 19.1 keV (pink curve).

The storm on March 15 – 20, 2013 was modeled with IMPTAM. Data on low energy electron fluxes from several satellites in the inner magnetosphere were available for this storm period. For IMPTAM validation, we primarily used the electron fluxes with energies from 5 to 50 keV for our analysis. These energies are most important for surface charging. We focused on the results for AMC 12 measurements at geostationary orbit. We focused on that data set in order to conduct an independent validation of the IMPTAM performance, since the coupled VERB-IMPTAM is validated inside geostationary orbit using the data from the Van Allen Probes.

AMC 12 geostationary satellite is at 322.5 degrees East. It has a CEASE II (Compact Environmental Anomaly Sensor) instrument (Dichter et al., 1998), which contains an electrostatic analyzer (ESA) and is a suite of various sensors intended to measure the in-situ space environment at the host spacecraft. The instrument contains a Lightly Shielded Dosimeter, a Heavily Shielded Dosimeter, a Particle Telescope (measuring high-energy electrons and protons), and an electrostatic analyzer for measuring low-energy electron fluxes in 10 channels, covering the range $5-50$ keV.

Figure 4.4 presents the electron fluxes at geostationary orbit observed by the CEASE II ESA instrument onboard the AMC 12 satellite by thick black lines and modeled with IMPTAM for (a) 39.7 – 50.7 keV (thin black line), (b) 31.1 – 39.7 keV (blue line), (c) $24.3-31.1$ keV (green line), (d) $19.1-24.3$ keV (red line), and (e) $15.0-19.1$ keV (pink line) during the storm on March $15-20$, 2013. The satellite's midnight (0230 UT) and noon (1430 UT) are marked with blue and yellow vertical lines, respectively. The end of each day is marked by black vertical line. The data are provided in the format of time-averaged differential fluxes (1/(cm^2 s sr eV)). The output from the model is integral flux (1/(cm^2 s)) produced by all electrons coming from all directions with energies in the ten given energy ranges. In order to be able to compare the observed and modeled fluxes more properly, we need to introduce the width of the energy channel and the solid angle 4π. So, the model electron fluxes are in model flux/($4\pi\Delta E$).

As it can be seen from Figure 4.4, the modeled fluxes follow reasonably well the observed ones. During the main phase of the storm on March 17th, many variations are reproduced, although the modeled fluxes are higher (the difference can reach an order of magnitude) on the day side than the observed. During the recovery phase of the storm on March 18th and 19th, the modeled fluxes drop much faster than the observed ones when the satellite moves to the dusk via noon. This discrepancy is due to the parameterizations we used for the electron losses due to interactions with specific types of waves, such as chorus waves (Orlova and Shprits, 2014) and with hiss waves (Orlova et al., 2014, 2016). The way how the electron lifetimes were parameterized with the same coefficients for all Kp values and for wide energy range may be the reason of the disagreement between the modeled and the observed fluxes. Moreover, the simple combination of the electron lifetimes due to chorus and hiss waves has non-smooth transitions between them at the location where lifetime due to chorus goes into the lifetime due to hiss. In addition, transitions between MLT-sectors inside both models are also with some jumps. This also can lead to rather complicated behavior of modeled fluxes. Although the very detailed dynamics of observed fluxes was not fully reproduced, the representation for electron lifetimes for keV electrons obtained from the VERB code is the best available model at present. The keV electron fluxes vary significantly on the time scales of tens of minutes. The electron lifetimes parameterized by 3-hour Kp index do not reflect the full picture of shorter time variations.

Output from IMPTAM modeling to VERB

The IMPTAM output for VERB was provided as 4D arrays of electron flux in (cm^2 s sr keV)$^{-1}$ in (L, MLT, pitch angle, energy). The original files from IMPTAM contain phase space density f as 4D array [radial distance, longitude, B/Beq (ratio between local magnetic field and magnetic field at the equator on the corresponding field line), particle magnetic moment]. Magnetic moment is the innermost index. The dimension of the array is $(31 \times 60 \times 26 \times 46)$. All explanations are in the headers of each file, output is provided every 30 minutes during the simulation of the entire storm on March $15 - 20$, 2013. The header example looks as:

```
<header
  step="480" INSIDE STEP
  timeRun="57600" TIME IN SECONDS
  time="1054224000"> UNIX TIME
   <data type="grid">
    <grid
    info="Rs, Re" RADIUS, ACTUALLY, L*, UNITLESS
    node="{1 30 3 9}"> 1-LINEAR GRID, 30-NUMBER OF INTERVALS IN R, 3-RMIN,
   9-RMAX
    <grid
      info="Longitude, deg" LONGITUDE, LONGITUDE=0 AT NOON
      node="{3 60}"/> FROM 0 TO 2PI, 60-NUMBER OF INTERVALS IN LONGITUDE
  </grid>
  <data
    Type="grid">
    <grid
      info="B/Beq, #" USED FOR 2nd INVARIANT AND PITCH
          ANGLE, 1- PA OF 90 DEG
      node="[1 1.04 1.09648 1.31826 1.58489 1.90546 2.29087 2.75423 3.31131
     3.98107 4.7863 5.7544 6.91831 8.31764 10 12.0226  14.4544 17.378 20.893
     25.1189 30.1995 36.3078 43.6516 52.4807 63.0957 75.8578]">
     <grid
        info="MagMoment, keV/nT" MAGNETIC MOMENT, NOT ENERGY
        node="{2 45 0.002 6}"/> 2-LOG, 45-INTERVALS, 0.002-MIN, 6-MAX
    </grid>
    <data
      type="unit"
      info="phaseden, f"/>
          MULTIPLY F BY ENERGY TO HAVE FLUX IN 1/CM2 S SR KEV
    </data>
  </data>
</header>
```

After initial coupling efforts, we replaced the grid in B/Beq with the grid in pitch angles and the grid in particle magnetic moment with the grid in particle energy to for simplifications. The final files which were used in VERB-IMPTAM coupling had the format as following:

```
<header
 step=”60”
 timeRun=”7200”
 time=”1363312800”>
   <data
               type=”grid”>
              <grid
                          info=”Rs, Re”
                          node=”{1 30 3 9}”>
                         <grid
                                info=”Longitude, deg”
                              node=”{3 40}”/>
         </grid>
           <data
                        type=”grid”>
                      <grid
                                  info=”PitchAngle, deg”
                              node=”[90 88 86 84 82 80 78 76 73 70 67 64 60
                                      55 50 45 40 35 30 25 20 15 10]”>
                              <grid
                                      info=”Energy, keV”
                                  node=”{2 20 1 100}”/>
                     </grid>
                       <data
                          type=”unit”
                              info=”flux, 1/cm2*sec*keV*sr”/>
          </data>
     </data>
</header>
```

Figure 4.5 presents the example of the IMPTAM output provided for the VERB-IMPTAM coupling. It shows the omnidirectional electron flux at 10 keV energy for March 17, 2013 when the main storm phase occurred. We can see very intense flux at 08 UT when the Dst was dropping. Between 09 − 12 UT, when Dst reached its first minimum, the flux maps also exhibited a clear increase in the electron flux at dawn where the electrons move to when they come from the plasma sheet toward the inner magnetosphere. Another intensification is seen at 19 − 20 UT, close to the second dip in Dst. Then, the electron flux starts to decrease when the storm recovery progresses. This behavior is very reasonable for the storm time variations of the keV electron fluxes.

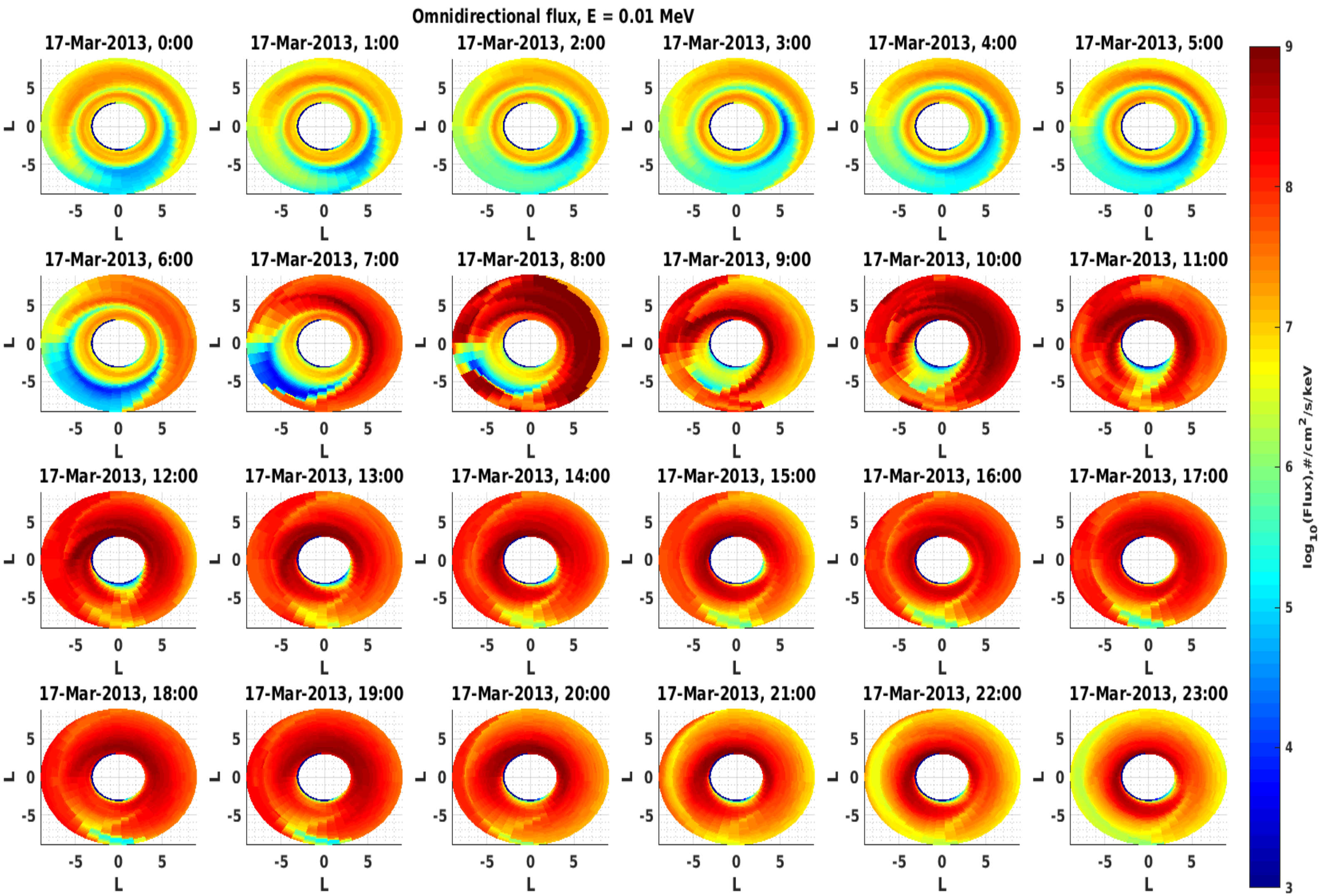

Figure 4.5: Example of the IMPTAM output for the 17th of March 2013. Displayed are omnidirectional electron fluxes at 10 keV energy for each hour of the day. Hour times are given in universal time (UT).

4.2 Preparation of boundary conditions

The electron distribution modeled by IMPTAM, as previously described, provides a low energy seed population for radiation belts electrons of higher energies, that can be implemented in the VERB simulations. In order to account for the dynamics of these low energy particles, the low energy and upper L^* boundary conditions needed for the VERB simulations were extracted from the time-dependent IMPTAM computations.

Extraction of the low energy boundary

IMPTAM modeled fluxes were delivered in a (L, MLT, α, E)-grid of $(31 \times 39 \times 23 \times 21)$ points for each hour of the entire simulation period $(15-20$, March, 2013). L has a range of 3 to 9 R_E, the MLT (magnetic local time) range is 0° to 360°, equatorial pitch angles from 10° to 90° are computed and electrons with energies of 1 to 100 keV were modeled. These energy values increase in a logarithmic scale in the IMPTAM grid. However, the boundary conditions we want to use as input for VERB must be given in the same computational grid of the code, i.e. (L^*, E, α; see Section 2.1). Table 4.3 summarizes the main parameters of grids used by IMPTAM and VERB, allowing an overview of their main differences. Contrary to IMPTAM, the VERB code operates in a MLT-independent grid. For this reason, the first step was to determine which MLT-averaging has the best agreement with the satellite data. We calculated MLT-averages over the night sector and over all MLT sectors, but the difference between them was less than 0.3 orders of magnitude. Therefore, we decided to build the boundaries using the averages over all MLT sectors.

Boundary	*IMPTAM*	*VERB-3D*
Radial Boundary	$L = 3-9$ R_E	$L^* = 1-6.6$ R_E
Pitch angle (α_0)	$\alpha_0 = 10° - 90°$	$\alpha_0 = 0° - 90°$
Magnetic local time (MLT)	$MLT = 0° - 360°$	MLT-independent
Energy (E)	$E = 10 - 100$ keV	Shown in Figure 2.1

Table 4.3: Overview of the computational grids of both models, IMPTAM and VERB.

The next processing step was the extraction of the IMPTAM modeled fluxes at 90° pitch angle. For these particles the second adiabatic invariant (J) is zero, which will greatly simplify our calculations. Also, in order to save computational time and on the basis that this is our initial trial coupling model, we used a dipole approximation and allowed $L^* = L$, i.e. from here on, radial distances in IMPTAM (L) are equal to the adiabatic radial distances in VERB (L^*). For the forecast tool and future work, this will be corrected using proper L^* tracing. IMPTAM-fluxes processed to this point are MLT-independent and at 90° pitch angle, laying on a ($L^* \times$ E) grid. Further adaptation of the output of IMPTAM to the VERB grid was done by extending modeled electron fluxes below $L^* = 3$ at all energies. For this, a fast exponential decay of the last IMPTAM flux value ($L^* = 3$, E) for each energy point E was used. Fluxes of particles with energies $E > 100$ keV at all L^* were computed similarly, but using the last IMPTAM flux value (L^*, $E = 100$ keV) for each L^*. As a final step, the processed IMPTAM output was interpolated to match the resolution of the VERB grid.

Figure 4.6 presents processed IMPTAM fluxes for electrons with 100 keV energy and at 90° equatorial pitch angle. Panel a) shows satellite data from GOES and Van Allen probes, and panel b) depicts IMPTAM fluxes interpolated onto a 2D (L^*, E)-grid that matches the points of the computational grid of the VERB code. Although, overestimation of fluxes during pre-storm times (from the 15th to the early hours of the 17th of March) mostly around $L^* = 4$ can be observed in the illustration, electron fluxes observed during the storm time and recovery phase are in very good agreement with the satellite observations.

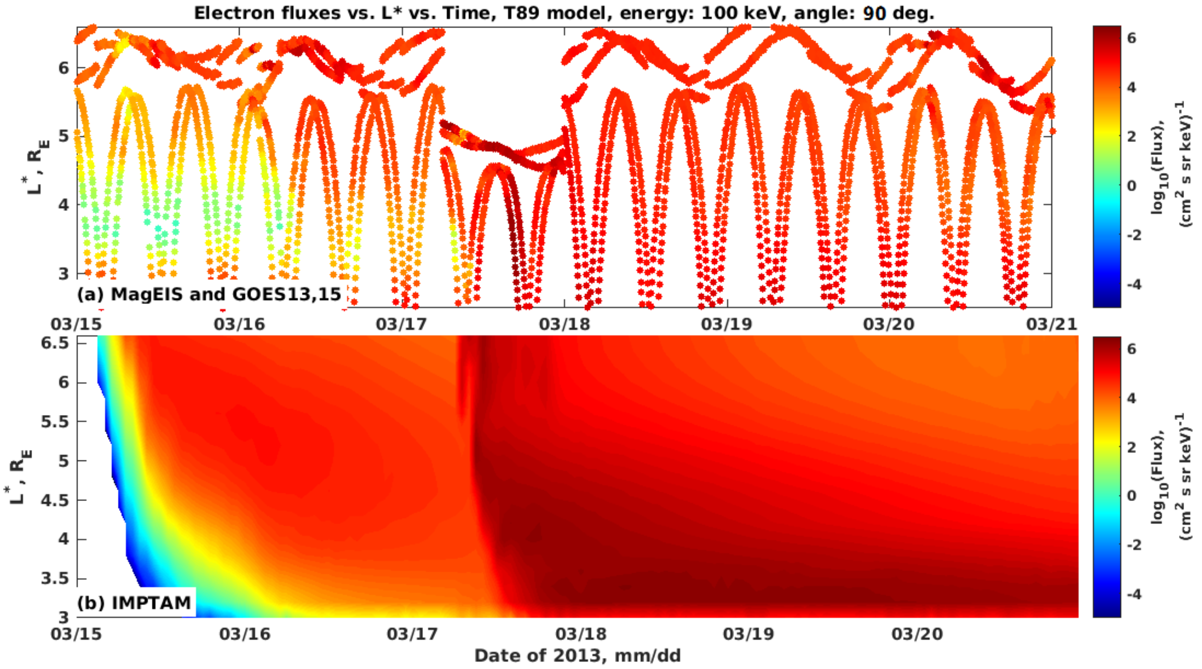

Figure 4.6: Electron fluxes for 100 keV electrons at local pitch angle $\alpha = 90°$ as function of L^* and time. a) Satellite observations from MagEIS and MagED, b) Electron fluxes computed in the new IMPTAM-grid matching the points of the computational grid of the VERB code.

The low energy boundary of the VERB code is located at $\mu_{min} = 10,2735$ MeV/G, as mentioned in section 2.1. Using equation (4), we can calculate μ for each point of the new IMPTAM grid for 90° pitch angle. Flux points matching the minimum μ condition ($\mu_{IMPTAM} = \mu_{min}$) are extracted together with their corresponding L^* component ($Flux_{IMPTAM}(L^*)$). Finally, in order to add a realistic pitch-angle distribution, we assumed a sinusoidal dependence of the pitch angles:

$$Flux_{BC}(L^*, \alpha_0) = Flux_{\mathrm{IMPTAM}}(L^*, \alpha_0 = 90^\circ) \cdot sin(\alpha_0), \tag{10}$$

where α_0 is a pitch angle point in the VERB-grid. Equation 10 defines IMPTAM fluxes extracted for the low energy boundary condition ($Flux_{BC}$) of VERB. Processed IMPTAM fluxes at minimum ($Flux_{BC}$) have to be converted to PSD values (PSD_{BC}), since this is the input the VERB code allows. This is done as follows:

$$PSD_{BC}(L^*, \alpha_0) = Flux_{BC}(L^*, \alpha_0)/pc^2(\mu_{min}), \tag{11}$$

where PSD_{BC} only depends on L^* and α_0, and pc^2 is calculated in dependence of μ_{min}. The calculated PSD values for each hour are written into a file, that is read by the VERB code at each step of the simulation.

Extraction of the upper L^* boundary

The boundary condition at $L^* = 6.6$ will provide a source for the low energy seed population (Drozdov et al., 2015) in our VERB simulations. Here, this boundary is time dependent and based on IMPTAM computed fluxes. We are mainly interested in the flux evolution of electrons at energies around 0.4 to 1 MeV, as this is the main energetic electron population of the upper radiation belt. For the calculation of the upper L^* boundary condition, we followed the approach of Brautigam and Albert (2000), who proposed scaling the electron flux distribution at the upper L^* boundary by multiplying it with an energy independent boundary flux ($B_f(t)$) to reproduce a realistic variation of the electron seed population.

We extracted the electron fluxes of the IMPTAM output with coordinates ($L^* = 6.6$, $E = 100$ keV, $\alpha_0 = 90^\circ$) for each hour of the simulation period. Electrons of 100 keV energy were chosen, because this is the highest energy available in the IMPTAM grid and therefore the closest to 1 MeV. The fluxes are then converted to PSD values (PSD_{IMPTAM}) using equation (11) for $E = 100$ keV. Using the time variations of these IMPTAM simulated PSD at 100 keV energy, we can modulate the time variations of fluxes at higher energies. For that, we calculate the average PSD (PSD_{IMPTAM}) for 100 keV electrons at $L^* = 7$ and its adiabatic transport to geostationary orbit ($L^* = 6.6$). This is done by calculating the steady state solution of the radial diffusion equation (see equation (9) at $L^* = 6.6$, and for Kp= 3 and $\tau = 1.2121$. We can relate these PSD values to higher energies using a statistical model of the long term PSD spectrum of electrons measured by the LANL satellites at $L^* = 7$ Re (Shprits et al., 2009b). Here, the averaged PSD values for 100 keV electrons (PSD_{IMPTAM}) are divided by the long-term averaged shape of the PSD-spectrum measured at $L^* = 7$ (PSD_{ave}), following Drozdov et al. (2015). The ratio

$$B_f(t) = PSD_{\mathrm{IMPTAM}}(t)/PSD_{ave}$$

of the modeled and the average PSD at 100 keV is a scaling factor $(B_f(t))$ that defines the energy -independent variation of the upper radial boundary. This time-dependent array is also saved in a file, that will be used by the VERB code at each step of the simulation. PSD values calculated by the VERB code at $L^* = 6.6$ are multiplied by the boundary flux $(B_f(t))$ at the corresponding simulation time (t). The extracted boundary conditions will be presented and described in the next section, together with the detailed explanation of the initial coupled simulations.

5 Coupled Simulation

For the simulations with the VERB code, six boundary conditions must be specified. Accounting for different physical assumptions, we derived four of these conditions, as explained in Section 2.1 (s. Table 2.2). With the aim to analyze how the low energy electron seed population influences the dynamics of high energy electrons in the upper radiation belt, it is important to use realistic time dependent PSD-values at the low energy and the upper L^* boundaries. In this study, these two boundary conditions have been obtained from simulations of the IMPTAM code and used as input for the VERB code simulations. In order to have a base for comparison, a non-coupled VERB simulation for the period of March 15th to 20th, 2013 was performed. In Section 5.1 the results of an initial coupled simulation using IMPTAM calculated PSD only at the low energy boundary are presented and compared with satellite data and the VERB stand-alone simulation. The coupled model including both boundary conditions from IMPTAM is described and analysed against satellite data and the non-coupled VERB simulation in section 5.2.

5.1 Stand-alone VERB simulation

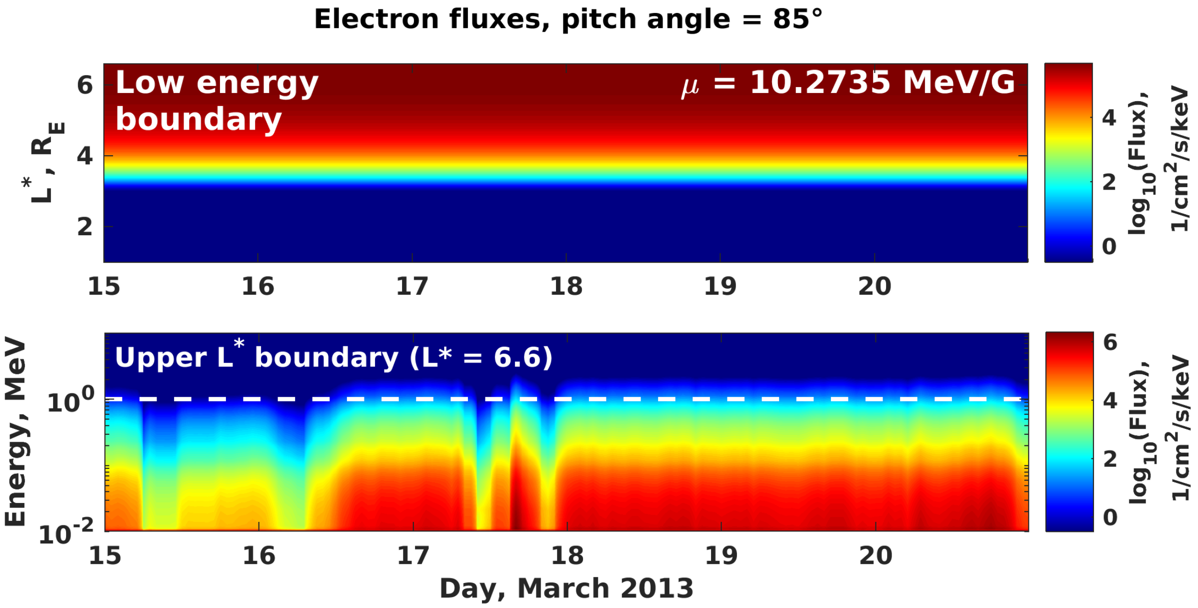

Figure 5.7: Electron fluxes at local pitch angle $\alpha_{loc} = 85°$ as function of time for the two boundary conditions used for a non-coupled VERB simulation. Upper panel: low energy boundary ($\mu = 10.2735$) calculated as the steady state solution of the radial diffusion equation. Lower panel: upper radial boundary ($L^* = 6.6$) estimated from satellite data after Drozdov et al. (2015). White dashed line marks 1 MeV energy.

Before coupling IMPTAM and VERB, a non-coupled VERB simulation was conducted using the parameters described in Section 2.1. The electron fluxes for the low energy and upper L^* boundary conditions are calculated as proposed by Drozdov et al. (2015) and presented in Figure 5.7 for particles at 85° pitch angle. Hereafter, the low energy boundary condition (Figure 5.7, upper panel) was set constant in time and equal to the initial PSD value, representing a balance between convective source and local losses (Shprits et al., 2009a). At the upper radial boundary (Figure 5.7, lower panel) PSD values are equal to the initial PSD at $L^* = 6.6$, which is then multiplied by a time dependent scaling factor that accounts for satellite observations and the long-term PSD spectrum measured at $L^* = 6.6$ for 1 MeV electrons.

As observed in Figure 5.7 (lower panel), on the first half of the 15th of March, a minor storm produces a flux dropout. Also, at the beginning of March 16th, a similar small event leads to a truncation of electron fluxes. Between these two minor storms, electron fluxes do not fully recover the initial magnitude. Prior to the main geomagnetic storm (March 17th), boundary fluxes show only minor variations. On the day of the storm, the first breakdown of fluxes is observed around midday and then followed by a flux recovery of short duration. Then, what appears to be a second dropout, but of less intensity is quickly followed by a strong flux enhancement that decays after a couple of hours, until a third dropout takes place. After this last rupture of electron fluxes, electromagnetic activity is rather quite.

Figure 5.8 (raw a) shows satellite measurements from Van Allen probes and GOES, together with the resulting electron fluxes from our non-coupled VERB simulation (Figure 5.8.raw b), for electrons at 85° pitch angle. Each column of the figure displays the data for particles of different energies, from left to right (f.l.t.r): I) 0,06; II) 0,1; III) 0,4; IV) 0,9 MeV, respectively. During the first day of the simulation period, computed electron fluxes for energies below 500 keV (Fig.5.8.b, columns I-III) around $L^* = 4 - 5$ are about 3 orders of magnitude higher than measured fluxes (Fig.5.8.a, columns I-III). This might be related to the time VERB simulations need to stabilize all the diffusion processes. For 900 keV particles (Fig.5.8.b, columns IV), the simulation results are very similar to the satellite observations (Fig.5.8.a, columns IV). The fluxes simulated for the day prior to the storm are in general good agreement with the satellite data. However, for electrons with energies of 400 keV minor overestimation of fluxes is observed.

The main phase of the second storm is characterized by two intense injections of particles with subsequent dropouts observed at all energies. Here, increased ULF-wave activity triggered inward radial diffusion, which transports electrons at high L^* to $L^* \approx 3 - 4$. These injections are well correlated with the flux dropouts observed in the upper-L^* boundary (Fig.5.7, lower panel). Local acceleration can be recognized after each injection as a peak in electron fluxes around $L^* = 4$. Such features are common in the recovery phase of geomagnetic storms and are caused by wave-particle interactions with chorus waves. Storm-time and recovery phase fluxes are well reproduced by our VERB standalone simulation, but some overestimation can be observed at higher energies (Fig.5.8.b, columns III,IV). Nevertheless, our non-coupled VERB simulation is able to reproduce all main features of the studied geomagnetic event, s.a. inward motion of fluxes during the main phase and flux buildup in the recovery phase.

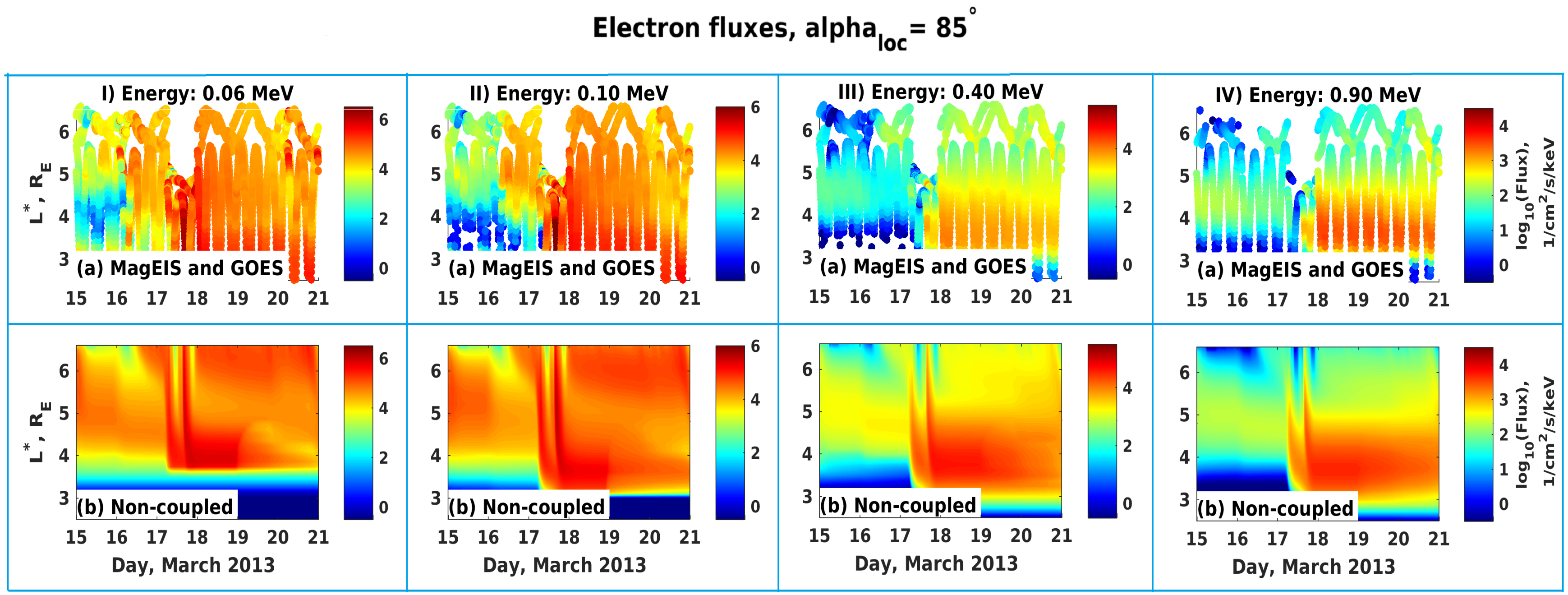

Figure 5.8: Each column displays electron fluxes as a function of L^* and time for local pitch angle $\alpha_{loc} = 85°$ at fixed energies: I) 0.06 MeV, II) 0.10 MeV, III) 0.40 MeV and IV) 0.9 MeV, respectively. The panels in each column show: a) Van Allen probes and GOES data, b) stand-alone VERB simulation. Note: color bars are different for each column.

5.2 Low-Energy Boundary

Application of constant low energy boundary fluxes in radiation belt simulations is only a good assumption when convective sources and local losses are in dynamic balance. However, this is not the case during storm times. Furthermore, low energy fluxes are known to be subject of time variations of even one order of magnitude (Jordanova and Miyoshi, 2005; Li et al., 2010). Introduction of fluxes simulated by IMPTAM at the low energy boundary of our VERB simulations allows to account for such variations and to model realistic dynamics of the low energy electron population in the outer radiation belt. In this initial coupled simulation, we only tested the effect of the low energy boundary fluxes estimated by IMPTAM and used the upper L^* computed from satellite observations that was described in the previous section (see Section 5.1, Fig.5.7, lower panel). Electron fluxes of both boundary conditions are presented in Figure 5.9 for electrons at 85° equatorial pitch angle. The upper panel shows the low energy boundary extracted from IMPTAM simulations at $\mu \approx 10,3$ MeV/G, which corresponds to about 10 keV at $L^* = 6,6$, and the lower panel shows fluxes at the upper L^* boundary ($L^* = 6,6$) (same as Fig.5.7, lower panel).

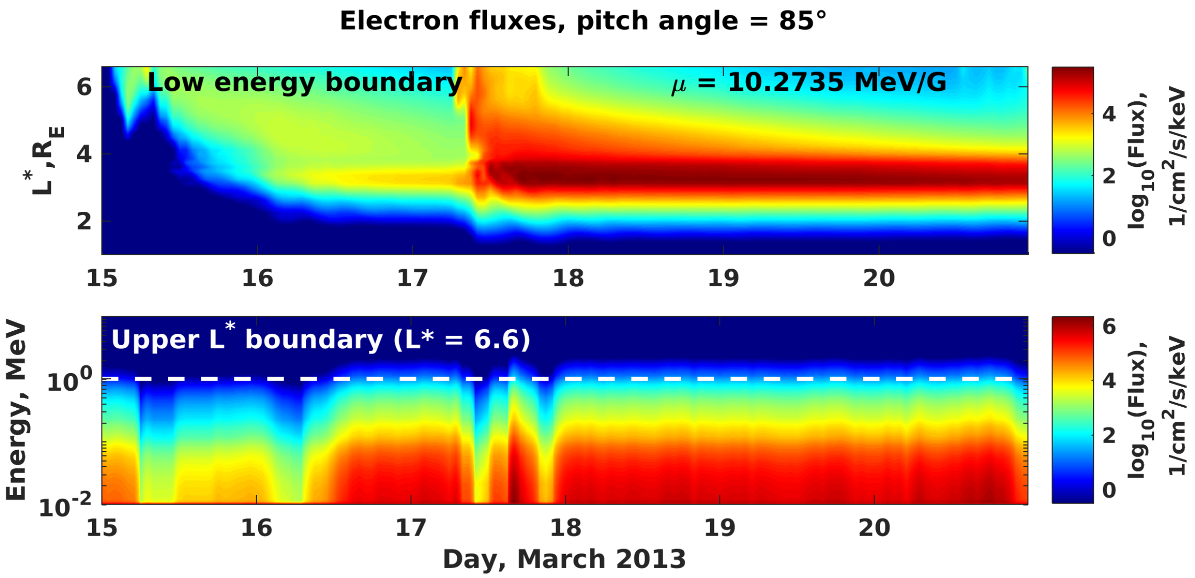

Figure 5.9: Electron fluxes at local pitch angle $\alpha_{loc} = 85°$ as a function of time for the two boundary conditions used for the first VERB-IMPTAM coupled simulation. Upper panel: low energy boundary ($\mu = 10.2735$) provided from IMPTAM simulations. Lower panel: upper radial boundary ($L^* = 6.6$) estimated from satellite data after Drozdov et al. (2015). White dashed line marks 1 MeV energy.

After a minor increase during the first half of March 15th, electron fluxes, which were mainly below $L^* = 5$ start increasing gradually up to about 3 orders of magnitude higher and reach $L^* \approx 3$. The fluxes observed at the beginning of the simulation period, might arise due to the fact that IMPTAM simulations start with an empty magnetosphere, which is continuously filled up and stabilized in the initial hours of the computation. On the 16th of March, fluxes reach a global maximum around $L^* = 3$ indicating particle transport to inner regions of the radiation belt environment. The value of this global

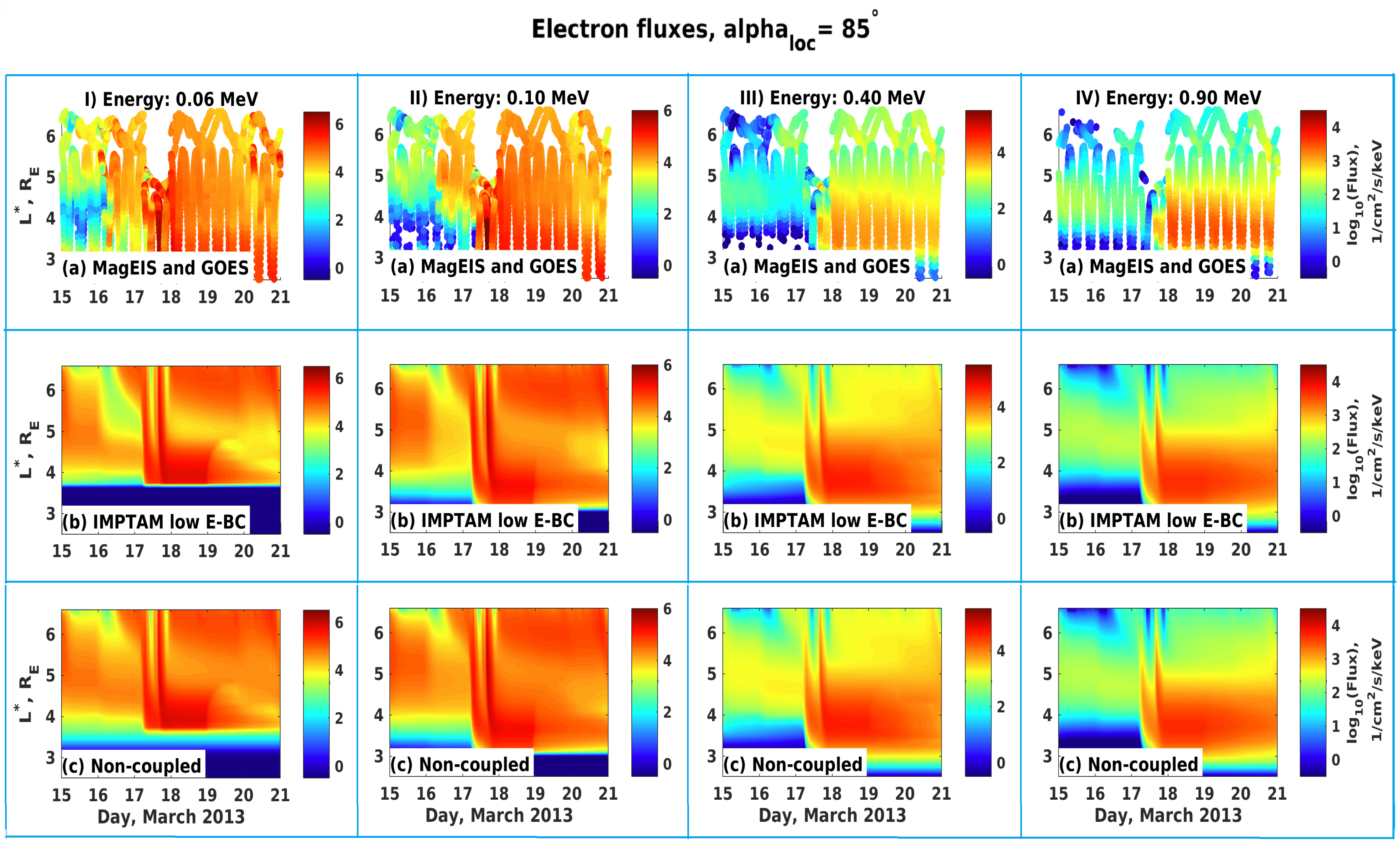

Figure 5.10: Each column displays electron fluxes as a function of L^* and time for local pitch angle $\alpha_{loc} = 85°$ at fixed energies: I) 0.06 MeV, II) 0.10 MeV, III) 0.40 MeV and IV) 0.9 MeV, respectively. The panels in each column show: a) Van Allen probes and GOES data, b) IMPTAM low E-BC = coupled simulation using IMPTAM's low energy boundary condition, c) Non-coupled = stand-alone VERB-3D simulation driven with satellite data and a constant low energy boundary, coupled VERB-IMPTAM simulation using the low energy boundary provided
by IMPTAM. Note: color bars are different for each column.

maximum continues increasing throughout the pre-storm phase. During the storm (March 17th) however, particle injections from higher to lower L-shells take place over several hours. Here, radial transport is enhanced and fluxes increase by about two orders of magnitude around $L^* = 3$ during the recovery phase.

Figure 5.10 displays satellite data (panel a) for different energies (f.l.t.r.: I) 0,06; II) 0,1; III) 0,4; IV) 0,9 MeV, respectively) and the corresponding results of this coupled simulation (Fig.5.10, panel b). For easier visual comparison, we placed the results of our non-coupled VERB simulation (s. Section 5.1, Fig.5.8, panel b) in the panel below (Fig.5.10, panel c). Although, the low energy boundaries used in this simulation and in the non-coupled simulation are completely different, resulting electron fluxes of both simulation show high resemblance at all energies. Main storm features observed in our VERB stand-alone simulations are also present in this coupled simulation, suggesting that the use of the steady state solution of the radial diffusion equation for the low energy boundary at $\mu = 10,2735$ MeV/G is a valid assumption. For 60 keV particles (Fig.5.10.b.I), the simulated electron fluxes around $L^* = 4 - 5$ are about one order of magnitude lower than fluxes observed in the VERB stand-alone simulation (Fig.5.10.c.I). Similar differences are also observed at 100 keV (Fig.5.10.b.II), but not at higher energies. Assessment of flux changes at higher energies ($0,4$ and $0,9$ MeV) was made by calculating the logarithmic difference between resulting electron fluxes from both simulations, non-coupled and coupled with the low energy boundary only, as follows: $log_{10}(\text{IMPTAM low E-BC}) - log_{10}(\text{non-coupled})$. The results of this operation are displayed in Figure 5.11 and indicate a minor decrease of fluxes in the coupled simulation. Although such a decrease is in agreement with the satellite observations, it not only suggests a small overestimation of fluxes computed by the VERB stand-alone simulation, but also that the electron seed population with energies $\leq$ 100 keV, which is the maximum energy contained in the IMPTAM simulations, is only able to energize or influence the dynamics of high energy

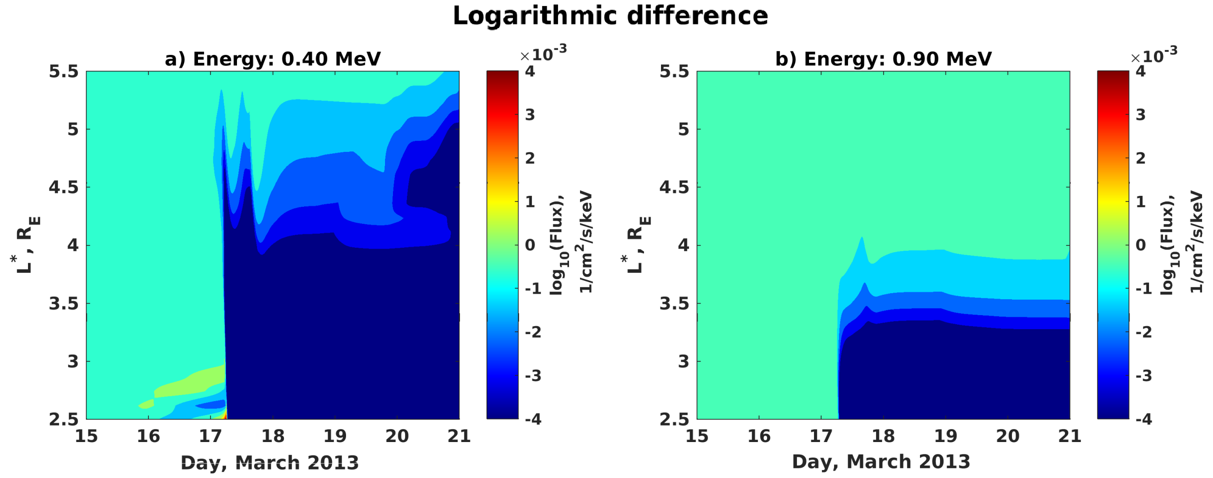

Figure 5.11: Logarithmic difference between electron fluxes resulting from the non-coupled and the first VERB-IMPTAM coupled simulations at higher energies $log_{10}(\text{IMPTAM low E-BC}) - log_{10}(\text{non-coupled})$, i.e. figure 5.10 (III and IV): a) 400 keV and b) 900 keV, respectively.

particles to a rather negligible extent. According to Horne et al. (2005), chorus waves cannot efficiently accelerate low energy electrons (with energies $\leq$ 300 keV), to MeV energies. Those low energy particles are therefore more subjected to losses than electrons with higher energies, which, on the contrary, can be accelerated to even higher energies during geomagnetic storms. As observed in the previous results and the non-coupled results (Section 5.1), the agreement of the resulting flux magnitudes is quite good.

5.3 Upper L^* Boundary

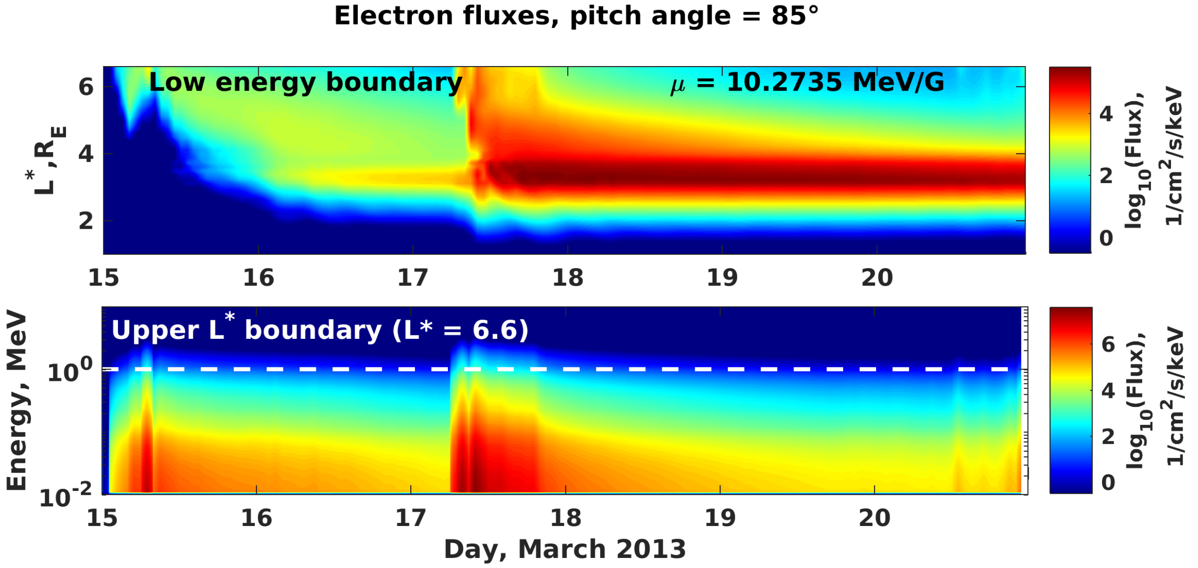

Figure 5.12: Electron fluxes at local pitch angle $\alpha_{loc} = 85°$ as a function of time for the two boundary conditions used for the second VERB-IMPTAM coupled simulation. Upper panel: low energy boundary ($\mu = 10.2735$) provided from IMPTAM simulations. Lower panel: upper radial boundary ($L^* = 6.6$) estimated using IMPTAM simulated fluxes. White dashed line marks 1 MeV energy.

Finally, to complete the coupling of IMPTAM and VERB, further dynamics of the seed population in the ring current were accounted for, by introducing IMPTAM-simulated electron fluxes at the upper L^* boundary ($L^* = 6.6$ Re) of our VERB computations. The fluxes used at the low energy boundary are the same as in the simulation described in Section 5.2., and also estimated by IMPTAM. Figure 5.12 presents both time-varying electron fluxes incorporated at the two boundaries in question, Figure 5.12 (upper panel) shows the low energy boundary (same as Fig.5.9, upper panel) and Figure 5.12 (lower panel) displays the upper L^* boundary. At the upper L^* boundary, strong injections of low energy particles (max. 100 keV) are observed during the first half of the 15th of March. These were triggered by the small geomagnetic event that took place early that day (s. Section 3) and although transport of high energy particles is also involved here, fluxes for energies above 100 keV are rather moderate, and for energies around 1 MeV even very low. After this initial storm, electron fluxes at all energies decrease, but this drop is specially strong for fluxes of particles with energies below 100 keV. On the storm day, two subsequent flux increases occur, indicating motion of low and high energy (even above 1 MeV) particles from the upper L^* boundary to lower L-shells. Fluxes of electrons with energies of up to some 100s of keV are high to moderate, while fluxes of particles with higher energy are rather low. In the recovery phase, electron fluxes maintain for several hours levels that are higher than those of quiet-times, until shortly before the beginning of March 18th, fluxes start decreasing.

Fluxes modelled with this coupled simulation are presented in Figure 5.13 (raw b) for particles at 85° pitch angle and for different energies (f.l.t.r.: I) 0,06; II) 0,1; III) 0,4; IV) 0,9 MeV, respectively). The corresponding satellite observations from GOES 13,15 and Van Allen Probes are shown in Figure 5.13(raw a). The coupled model is able to reproduce well the general shape and increase of electron fluxes throughout the simulation. Fluxes simulated for the first day (March 15th) are well recreated for particles with $0,9$ MeV energy for all L^*-values below 6 (Fig.5.13.b.IV). For lower energies, simulated fluxes are overestimated by about 1 to 4 orders of magnitude. During the first half of that day, a particle injection related to the minor geomagnetic storm on that day is reproduced. Particles energized by this event are transported to lower L^* and generate the observed overestimation. On the second day of simulation (March 16th), fluxes of low energy particles (Fig.5.13.b.I, II) are in good agreement with satellite data but still slightly overestimated. At higher energies (Fig.5.13.b.III, IV), excess of particles is observed as an enhancement of fluxes of up to two orders of magnitude. Storm-time fluxes and the maximum peak around $L^* = 4$ during the recovery phase show overestimation at all energies. However, recovery phase fluxes and the radial reach of the upper radiation belt are more amplified at energies above 300 keV.

Comparison with the previous simulations shows the strong influence the upper L^* boundary condition has on the VERB simulations. Although, the fluxes extracted from IMPTAM for this boundary and the fluxes estimated from satellite data are in the same orders of magnitude, they show completely different dynamics. Accounting for this and for the complexity of the coupled model, there could be several reasons for the observed differences between our coupled model, the satellite observations and our previous simulations: 1) loss mechanisms that in nature balance such inward radial transport are missing in IMPTAM and/or VERB, 2) the particle injection simulated for March 15th is overestimated by the ring current model, this might suggest missing dynamics in the code, and 3) the processing of the boundary fluxes extracted from IMPTAM, performed to accomplish the coupling, could have introduced biases in the boundary conditions.

Continuous overestimation of fluxes indicates excess of particles in the simulation, due to lacking loss mechanism that could balance enhanced inward transport of particles. For this reason, accounting for certain loss mechanisms in our simulations would improve our coupled model. Since flux overestimation is observed at all energies (Fig.5.13.b.I to IV), one eligible mechanism would be the magnetopause shadowing. During storm times, the pressure of the solar wind plasma pushes the magnetopause towards the Earth, leading

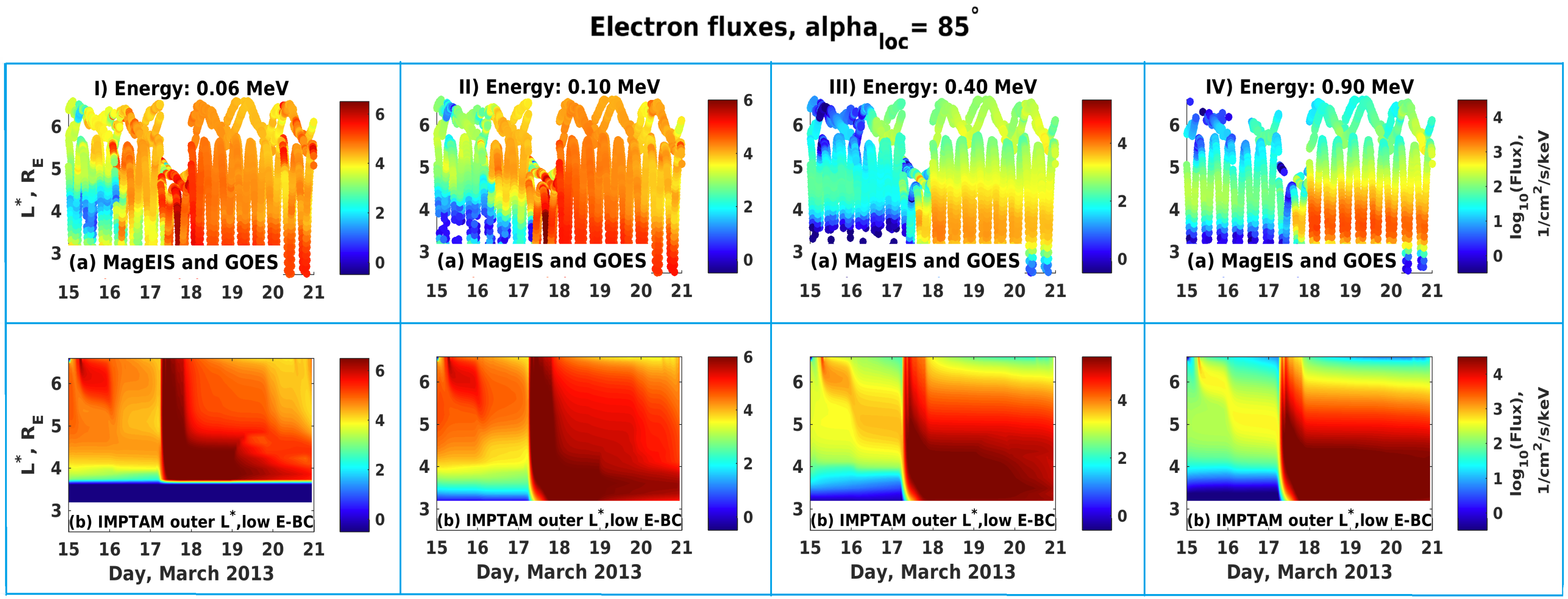

Figure 5.13: Each column displays electron fluxes as a function of L^* and time for local pitch angle $\alpha_{loc} = 85°$ at fixed energies: I) 0.06 MeV, II) 0.10 MeV, III) 0.40 MeV and IV) 0.9 MeV, respectively. The panels in each column show: a) Van Allen probes and GOES data, b) IMPTAM upper L*, low E-BC = coupled VERB-IMPTAM simulation using the low energy and upper L^* boundary provided from IMPTAM.

Note: color bars are different for each column.

to strong outward radial transport of particles. Introducing losses to the magnetopause could significantly improve our simulations.

Since the upper L^* boundary strongly influences VERB simulations, the dynamics of the ring current model should be as accurate as possible. The IMPTAM fluxes used at the upper L^* boundary of this simulation (Fig.5.12, lower panel) have the same orders of magnitude as the fluxes estimated from satellite observations (Fig.5.9, lower panel), but their evolution in time is completely different. Also, during the first day of this simulation, particle injections from the boundary are observed as flux enhancements at all energies. However, there is no evidence of such injections in the satellite observations. Missing processes in the IMPTAM code may have overestimated the fluxes for that particular event, but also could lead to unrealistic simulation results for other storms.

Data processing applied to the boundary condition included modeling an exponential decay for fluxes of high energy particles. This approach might be too inaccurate to describe the dynamics of such particles. Also, the scaling factor used for upper L^* boundary, was chosen based on the long-term PSD spectrum of 100 keV energy particles, because 100 keV was the highest energy delivered by IMPTAM simulations. This is a very vague approach, as it assumes similar behaviour of low and high energy particles for flux scaling. Extending the computational grid of IMPTAM to higher energies would allow a more realistic estimation of the upper L^* boundary condition. On the other hand, linear interpolation between grids can add biased values to our boundary data.

6 Conclusions

Initial coupled simulations of the IMPTAM and VERB codes have been performed. The aim of this report is to present the results of this initial coupling of both models. The IMPTAM code computes the dynamics of low energy electrons (up to 100s of keV) in the ring current, while the VERB code models flux evolution for electrons of up to some 10s of MeV, in the environment of the radiation belts. Low energy (10s of keV) particles can be accelerated by combined radial transport and local acceleration, thus influence the dynamics of high energy electrons. For this reason, coupling of ring current dynamics with diffusion processes allows recreation of realistic physical conditions in the radiation belt region, which in turn will generate accurate time dependent models.

In order to ease comparison, we computed a non-coupled simulation of VERB for the time period of the 15th-20st of March, 2013. The low energy boundary condition used in that simulation was constant in time and equal to the initial PSD value calculated as the steady state solution of the diffusion equation. The upper L^* boundary was calculated from satellite data. The resulting electron fluxes modeled with this boundary conditions have good agreement with satellite data and reproduce all important features of geomagnetic storms.

To test the effect of the low energy boundary, a preliminary simulation was performed using IMPTAM modeled fluxes at the lower energy boundary of VERB. The upper L^* for this simulation was estimated from satellite data, as in the non-coupled simulation. The results of this simulation were compared with satellite data and the VERB stand-alone simulation. Despite the differences between the chosen low energy boundaries, electron fluxes from this simulation are very similar to the ones from the non-coupled simulation at all energies and also agree well with the satellite observations. Both models reproduce flux enhancement at $L^* = 4$ during the recovery phase.

At lower energies (below 200 keV), fluxes around $L^* = 5$ are slightly lower than in the non-coupled simulation. The same is observed at higher energies, however, reduction of fluxes here reaches lower L^* and has rather negligible magnitude. This indicates, that for low energy particles realistic physical assumptions about the low energy boundary condition are particularly important. On the other hand, high energy particle dynamics appear to be rather insensitive to this boundary condition, probably because of their distance to this boundary in phase space. Therefore, assuming a dynamic balance between convective source and particle losses for the low energy boundary condition can be accurate enough to simulate fluxes of 400 to 900 keV energy electrons in the upper radiation belt.

The last coupled simulation performed, integrated IMPTAM simulated fluxes at the upper L^* boundary of VERB. For this simulation, also the low energy boundary from IMPTAM was used. This coupled model is able to reproduce the shape and general flux enhancement well during storm time and recovery phase, and for all energies. For energies below 400 keV, modeled fluxes during the recovery phase above $L^* = 4.5$ are in good agreement with satellite observations and previous simulations. At other energies and lower L^*, simulated fluxes show general overestimation, which is particularly pronounced during the recovery phase.

The VERB-IMPTAM coupled model could be improved in a number of ways, in order to obtain more accurate results. Inclusion of losses to the magnetopause could significantly improve the simulations, as it would help to balance the particle excess observed. Furthermore, missing dynamics or loss mechanisms in the IMPTAM code may lead to overestimated fluxes, such as observed in the particle injections on March 15th. Extending the energy range of the IMPTAM grid would also increase accuracy of the upper L^* boundary condition, because the highest energy of the IMPTAM simulations defines the scaling factor of the PSD-spectrum.

The coupled VERB-IMPTAM model is completely independent of satellite observations and only depends on solar wind parameters and Kp predictions. In this sense, the model is suitable as a forecasting tool for the electron dynamics in the radiation belts.

7 Future tasks and connection to other WPs

The results of the IMPTAM will be validated against satellite observations and will be also compared with the NARMAX predictions (Task 6.3 in WP6). Task 5.4 will result in developing of a trial version of forecast model for low energy electrons which will be part of Task 7.2 in WP7 for implementation of VERB-IMPTAM model in fusion of forecasting tools. On the other hand, further improvement of the VERB-IMPTAM model can be achieved. Increasing the energy spectrum in IMPTAM simulations will allow estimation of the long-term PSD spectrum for higher energies and thereby better computation of the upper radial boundary. Also, important improvement can be reached by including losses to the magnetopause in our VERB simulations.

8 Update: Model Improvement

We have been able to improve the couple VERB-IMPTAM model by changing some of the processing steps performed to extract the boundary conditions. In section 8.1, we briefly explain the changes in the methods that led to the overall improvement of the model and in section 8.2, we present the results of the final coupled model.

8.1 Improvement of the boundary conditions

The low energy boundary for the VERB code

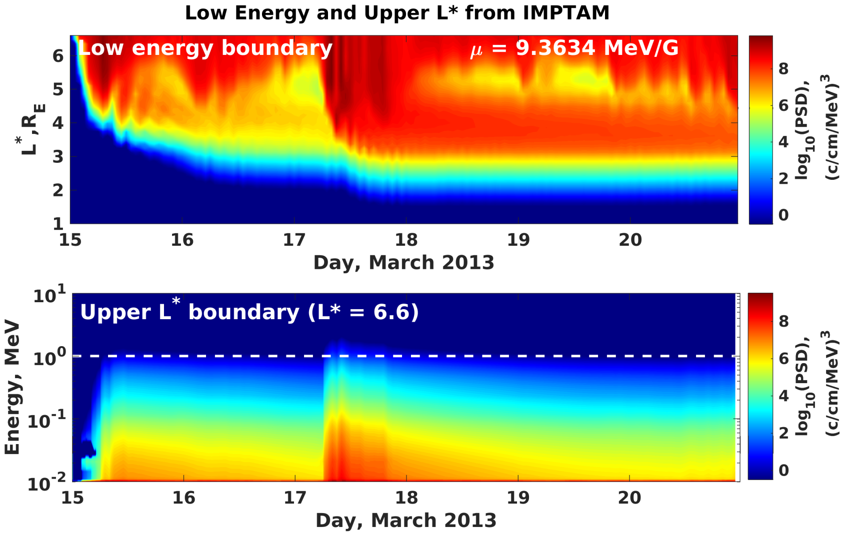

Figure 8.14: Evolution of electron PSD as a function of time for the two boundary conditions used for the fully coupled VERB-IMPTAM simulation. Upper panel: low energy boundary ($\mu = 9.3634$ MeV/G) provided from IMPTAM simulations. Lower panel: upper radial boundary ($L^* = 6.6$ at local pitch angle $\alpha_{loc} = 85°$) estimated using IMPTAM simulated fluxes. White dashed line marks 1 MeV energy.

In general, the extraction of the low energy boundary was performed in the same manner as explained in section 4.2. The only change made here was the location of the low energy boundary of the VERB code, the boundary was lowered to $\mu_{min} = 9.3634$ MeV/G, as this allows us to better resolve energies as low as 10 keV at $L^* = 6.6$. The new low energy boundary is presented in Figure 8.14 (upper panel) as the time varying PSD. At the beginning of the simulation the PSD values are very low, because IMPTAM simulations start with an empty magnetosphere that fills up and stabilizes during the initial hours of the simulation. After a moderate increase during the first half of March 15th, PSD values start increasing gradually and reaching lower L-shells, $L^* \approx 4$. Also on March 16th, a minor injection is also observed. These two events are well correlated with the depletions observed in the upper L^* boundary from satellite data and generate minor peaks in PSD around $L^* = 3 - 4$. This indicates particle transport to inner regions of the radiation belt environment, which will further affect the VERB simulations. During the main storm, particle injections from higher to lower L-shells take place over several hours. Here, radial transport is enhanced and the PSD increases by more than two orders of magnitude around $L^* = 3.5$. During the recovery phase PSD values at geosynchronous orbit return to quiet time levels, but the peak at $L^* = 3.5$ remains throughout the rest of the simulation, decaying only slowly.

Defining the low energy boundary at a low μ significantly improved this boundary condition, introducing more realistic dynamics and more detailed features of the electron flux evolution during enhanced geomagnetic activity. However, due to the low sensitivity of the energetic particles to the low energy boundary, the impact of this more realistic boundary is of rather small magnitude.

The upper L^* boundary for the VERB code

For the calculation of the upper L^* boundary condition, we followed the approach of Brautigam and Albert (2000), as explained in section 4.2. However, instead of extracting hourly electron fluxes computed with IMPTAM at: $L^* = 6.6$, $E = 100$ keV, $\alpha_0 = 90°$ and then building the average fluxes expected at higher energies from the long term PSD spectrum. We related the energy spectra of the low and energetic electron populations using a statistical model of the long term flux spectrum $Flux_{stat.model}$ of electrons measured by the LANL satellites at $L^* = 7$ Re (Shprits et al., 2009b). Knowing the low energy fluxes from IMPTAM at $L^* = 7$, we estimated the coefficients of an exponential fit between the spectrum and the output of IMPTAM at three point energies (100 keV, 1 MeV and 3 MeV). Once the fluxes at these key energies match the spectrum, electron fluxes between these reference energies are interpolated. This allows us not only to modulate but even reconstruct flux evolution at higher energies. Then using the adiabatic invariance of μ, we can calculate the fluxes of the target energies at $L^* = 6.6$. With this method, we account for the dynamics of the low energy seed population and the statistical data of energetic electrons. Since we only want the time variations of the upper boundary fluxes, with the estimated fluxes at 1 MeV, we calculate the scaling factor B_f, as follows:

$$B_f(t) = Flux_{\mathrm{IMPTAM}}(t)/Flux_{stat.model}.$$

B_f modulates the boundary fluxes of the VERB-3D simulations, as the initial PSD values calculated by the VERB code at $L^* = 6.6$ for each time step (t) are multiplied by $(B_f(t))$. Figure 8.14 (lower panel) presents the resulting time-varying PSD used at the upper L^* boundary. As displayed, moderate injections of low energy particles (max. 100 keV) are observed during the first half of March 15th. These were triggered by the small geomagnetic event taking place earlier that day and although transport of high energy particles is also involved here, the PSD for energies above 100 keV is rather low, and around 1 MeV even very low. After this initial storm, the PSD values at all energies decrease. On the storm day, two subsequent increases in PSD occur, indicating motion of low and high energy particles (even above 1 MeV) from the upper L^* boundary to lower L-shells. Electron PSD for up to some 100s of keV energies is high to moderate, while for particles with higher energy, the PSD values are rather low. In the recovery phase, the PSD maintains higher levels than those of quiet-times for several hours, before they start decaying at the beginning of March 18th.

Changing the method for the extraction of the upper L^* was very important and led to significant improvement of the coupled VERB-IMPTAM model. Boundary fluxes calculated with this approach are of lower magnitudes than the boundary fluxes calculated with the method explained in section 4.2. To a large extent, this boundary is the responsible for the high overestimation observed in the initial coupled model.

8.2 Improvement of the VERB-IMPTAM coupled model

Using the two improved boundary conditions presented in section 8.1, we have performed a fully coupled simulation with the VERB-IMPTAM model. Electron fluxes resulting from this fully coupled simulation are presented in Figure 8.15 (panel b) for different energies (different columns), together with the corresponding satellite observations of GOES and Van Allen Probes (panel a). The coupled model is able to reproduce well the general evolution of electron fluxes throughout the simulation. The two particle injections during the first half of March 15th and 16th related to minor geomagnetic storms are reproduced by the simulations at 60 and 100 keV energies (Fig.8.15.b.I, II). Particles energized by these events are transported to lower L^* and generate the observed overestimation of about 1 to 3 orders of magnitude is partly due to inaccuracies in the injections simulated by IMPTAM and also due to possible duplication of dynamics present in both models. However, the fluxes observed at $L^* > 5$ are in good agreement with the satellite data. At higher energies (Fig.8.15.b.III, IV), enhanced radial transport leads to an overestimation of fluxes of up to two orders of magnitude. Storm-time fluxes and the maximum peak around $L^* = 4$ during the recovery phase show overestimation at 60, 100 and 400 keV energies. However, electron fluxes at 900 keV are in the same order of magnitude as the measurements, showing only a slight overestimation of the radial extent of the belt and of the peak intensity during March 18th.

8.3 Final remarks

The preliminary VERB-IMPTAM model has been improved making small changes to the initial extraction methods of the boundary conditions. The improved model shows very good agreement with the satellite data for energetic electrons ($400 - 900$ keV) and can be used as forecasting tool. We should mention that although, the upper L^* boundary from IMPTAM and the one from GOES data are in the same orders of magnitude, their time evolution is not quite the same. The scaling factor used for upper L^* boundary was based an exponential fit of the long-term PSD spectrum at 100 keV electrons, as this was the highest energy in the IMPTAM grid. This is a very vague approach, as the scaling assumes a similar behaviour of low and high energy particles. Extending the computational grid of IMPTAM to higher energies would allow a more realistic estimation of the upper L^* boundary condition. Also, the injections on the first three days of the simulation are present in both boundaries, but the injections computed by IMPTAM show some overestimation. The model of the source distribution in the plasma sheet embedded in

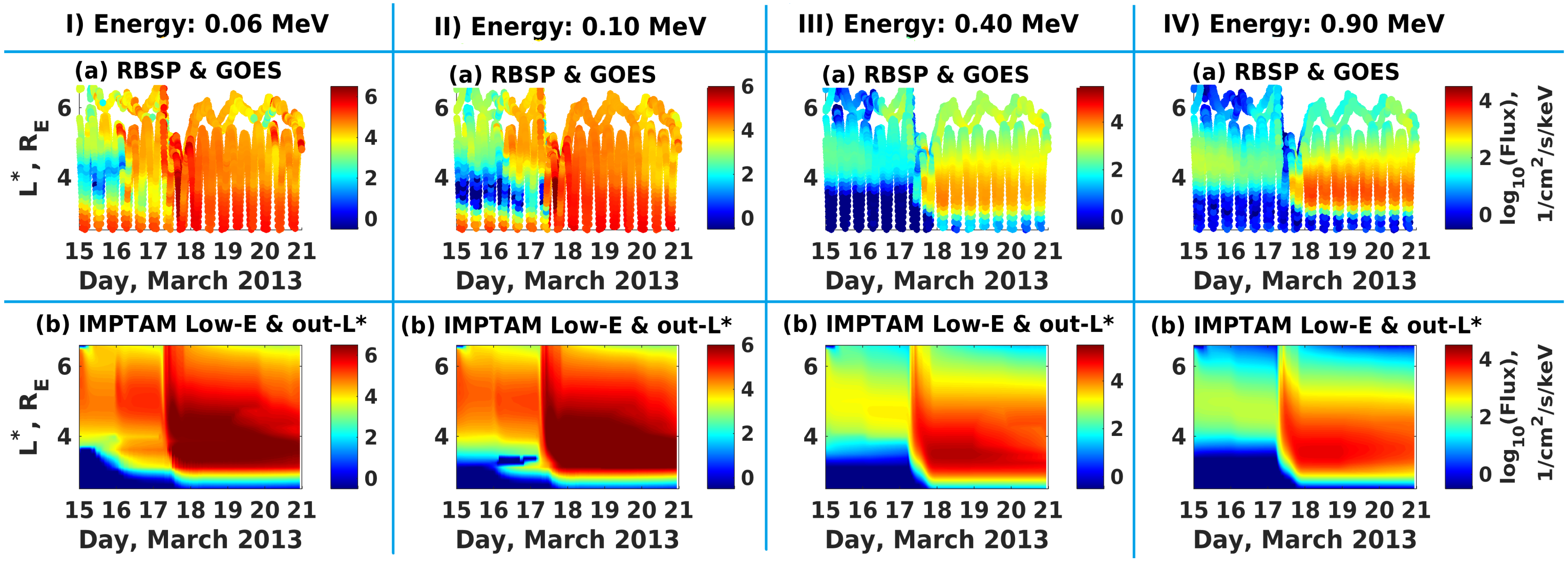

Figure 8.15: Electron fluxes as a function of L^* and time for local pitch angle $\alpha_{loc} = 85°$ at fixed energies: I) 0.06 MeV, II) 0.10 MeV, III) 0.40 MeV and IV) 0.90 MeV, respectively. The panels in each column show: a) Van Allen probes and GOES data, b) fully coupled VERB-IMPTAM simulation using the low energy and upper L^* boundary provided from IMPTAM. Note: color bars are different for each column.

IMPTAM is based on empirical relations with solar wind parameters and describes more accurately particles in the dawn sector. These restrictions could lead to the observed overestimation of injection fluxes.

Accounting the complexity of the used models, we can still find some room for improvement as mentioned above. Also as discussed in chapters 5 and 6, improving lifetime parametrizations and including losses to the magnetopause would further improve the coupled model. Nevertheless, the two main conclusions from this study are: 1) while the trapped low energy population (max. energy 100 keV) seems to affect the dynamics of electrons up to 400 keV energies, high energy particle ($>$ 900 keV) dynamics appear to be rather nonsensitive to this population; 2) unlike the low energy boundary, the upper L^* boundary does have a significant influence on energetic electron dynamics.

References

Abel, B. and Thorne, R. M. (1998). Electron scattering loss in earth's inner magnetosphere: 1. dominant physical processes. *Journal of Geophysical Research: Space Physics*, 103(A2):2385–2396.

Agapitov, O., Artemyev, A., Krasnoselskikh, V., Khotyaintsev, Y. V., Mourenas, D., Breuillard, H., Balikhin, M., and Rolland, G. (2013). Statistics of whistler mode waves in the outer radiation belt: Cluster staff-sa measurements. *Journal of Geophysical Research: Space Physics*, 118(6):3407–3420.

Albert, J. (2007). Simple approximations of quasi-linear diffusion coefficients. *Journal of Geophysical Research: Space Physics*, 112(A12).

Albert, J. and Young, S. (2005). Multidimensional quasi-linear diffusion of radiation belt electrons. *Geophysical research letters*, 32(14).

Albert, J. M., Meredith, N. P., and Horne, R. B. (2009). Three-dimensional diffusion simulation of outer radiation belt electrons during the 9 october 1990 magnetic storm. *Journal of Geophysical Research: Space Physics*, 114(A9).

Apatenkov, S., Sergeev, V., Kubyshkina, M., Nakamura, R., Baumjohann, W., Runov, A., Alexeev, I., Fazakerley, A., Frey, H., Muhlbachler, S., et al. (2007). Multi-spacecraft observation of plasma dipolarization/injection in the inner magnetosphere. In *Annales Geophysicae*, volume 25, pages 801–814. Copernicus GmbH.

Apatenkov, S., Sugak, T., Sergeev, V., Shukhtina, M., Nakamura, R., Baumjohann, W., and Daly, P. (2009). Radial propagation velocity of energetic particle injections according to measurements onboard the cluster satellites. *Cosmic Research*, 47(1):22–28.

Baker, D., Allen, J., Belian, R., Blake, J., Kanekal, S., Klecker, B., Lepping, R., Li, X., Mewaldt, R., Ogilvie, K., et al. (1996). An assessment of space environmental conditions during the recent anik e1 spacecraft operational failure. *ISTP Newsletter*, 6(2):8.

Baker, D. and Stone, E. (1978). The magnetopause energetic electron layer, 1. observations along the distant magnetotail. *Journal of Geophysical Research: Space Physics*, 83(A9):4327–4338.

Beutier, T. and Boscher, D. (1995). A three-dimensional analysis of the electron radiation belt by the salammbô code. *Journal of Geophysical Research: Space Physics*, 100(A8):14853–14861.

Boscher, D., Bourdarie, S., Thorne, R., and Abel, B. (2000). Influence of the wave characteristics on the electron radiation belt distribution. *Advances in Space Research*, 26(1):163–166.

Bourdarie, S., Boscher, D., Beutier, T., Sauvaud, J.-A., and Blanc, M. (1996). Magnetic storm modeling in the earth's electron belt by the salammbô code. *Journal of Geophysical Research: Space Physics*, 101(A12):27171–27176.

Bourdarie, S., Boscher, D., Beutier, T., Sauvaud, J.-A., and Blanc, M. (1997). Electron and proton radiation belt dynamic simulations during storm periods: A new asymmetric convection-diffusion model. *Journal of Geophysical Research: Space Physics*, 102(A8):17541–17552.

Boyle, C., Reiff, P., and Hairston, M. (1997). Empirical polar cap potentials. *Journal of Geophysical Research: Space Physics*, 102(A1):111–125.

Brautigam, D. and Albert, J. (2000). Radial diffusion analysis of outer radiation belt electrons during the october 9, 1990, magnetic storm. *Journal of Geophysical Research: Space Physics*, 105(A1):291–309.

Büchner, J. and Zelenyi, L. (1987). Chaotization of the electron motion as the cause of an internal magnetotail instability and substorm onset. *Journal of Geophysical Research: Space Physics*, 92(A12):13456–13466.

Carpenter, D. and Anderson, R. (1992). An isee/whistler model of equatorial electron density in the magnetosphere. *Journal of Geophysical Research: Space Physics*, 97(A2):1097–1108.

Craven, J. D. (1966). Temporal variations of electron intensities at low altitudes in the outer radiation zone as observed with satellite injun 3. *Journal of Geophysical Research*, 71(23):5643–5663.

Delcourt, D., Sauvaud, J.-A., Martin, R., and Moore, T. (1996). On the nonadiabatic precipitation of ions from the near-earth plasma sheet. *Journal of Geophysical Research: Space Physics*, 101(A8):17409–17418.

Denton, R., Menietti, J., Goldstein, J., Young, S., and Anderson, R. (2004). Electron density in the magnetosphere. *Journal of Geophysical Research: Space Physics*, 109(A9).

Denton, R., Takahashi, K., Galkin, I., Nsumei, P., Huang, X., Reinisch, B., Anderson, R., Sleeper, M., and Hughes, W. (2006). Distribution of density along magnetospheric field lines. *Journal of Geophysical Research: Space Physics*, 111(A4).

Dichter, B., McGarity, J., Oberhardt, M., Jordanov, V., Sperry, D., Huber, A., Pantazis, J., Mullen, E., Ginet, G., and Gussenhoven, M. (1998). Compact environmental anomaly sensor (cease): A novel spacecraft instrument for in situ measurements of environmental conditions. *IEEE Transactions on Nuclear Science*, 45(6):2758–2764.

Drozdov, A., Shprits, Y., Orlova, K., Kellerman, A., Subbotin, D., Baker, D., Spence, H. E., and Reeves, G. (2015). Energetic, relativistic, and ultrarelativistic electrons: Comparison of long-term verb code simulations with van allen probes measurements. *Journal of Geophysical Research: Space Physics*, 120(5):3574–3587.

Dubyagin, S., Ganushkina, N. Y., Sillanpää, I., and Runov, A. (2016). Solar wind-driven variations of electron plasma sheet densities and temperatures beyond geostationary orbit during storm times. *Journal of Geophysical Research: Space Physics*, 121(9):8343–8360.

Elkington, S. R., Wiltberger, M., Chan, A. A., and Baker, D. N. (2004). Physical models of the geospace radiation environment. *Journal of atmospheric and solar-terrestrial physics*, 66(15):1371–1387.

Fok, M.-C., Moore, T., Wilson, G., Perez, J., Zhang, X., Mitchell, D., Roelof, E., Jahn, J.-M., Pollock, C., Wolf, R., et al. (2003). Global ena image simulations. In *Magnetospheric Imaging—The Image Prime Mission*, pages 77–103. Springer.

Ganushkina, N., Pulkkinen, T., Milillo, A., and Liemohn, M. (2006). Evolution of the proton ring current energy distribution during 21–25 april 2001 storm. *Journal of Geophysical Research: Space Physics*, 111(A11).

Ganushkina, N. Y., Amariutei, O., Shprits, Y., and Liemohn, M. (2013). Transport of the plasma sheet electrons to the geostationary distances. *Journal of Geophysical Research: Space Physics*, 118(1):82–98.

Ganushkina, N. Y., Amariutei, O., Welling, D., and Heynderickx, D. (2015). Nowcast model for low-energy electrons in the inner magnetosphere. *Space Weather*, 13(1):16–34.

Ganushkina, N. Y., Liemohn, M., Amariutei, O., and Pitchford, D. (2014). Low-energy electrons (5–50 kev) in the inner magnetosphere. *Journal of Geophysical Research: Space Physics*, 119(1):246–259.

Ganushkina, N. Y., Liemohn, M., and Pulkkinen, T. (2012). Storm-time ring current: model-dependent results. *Ann. Geophys*, 30:177–202.

Ganushkina, N. Y., Pulkkinen, T., and Fritz, T. (2005). Role of substorm-associated impulsive electric fields in the ring current development during storms. In *Annales Geophysicae*, volume 23, pages 579–591.

Glauert, S. A. and Horne, R. B. (2005). Calculation of pitch angle and energy diffusion coefficients with the padie code. *Journal of Geophysical Research: Space Physics*, 110(A4).

Green, J. and Kivelson, M. (2001). A tale of two theories: How the adiabatic response and ulf waves affect relativistic electrons. *Journal of Geophysical Research: Space Physics*, 106(A11):25777–25791.

Hanser, F. (2011). Eps/hepad calibration and data handbook (tech. rep. goesn-eng-048d). carlisle, ma: Assurance technology corporation.

Horne, R. B., Glauert, S. A., Meredith, N. P., Koskinen, H., Vainio, R., Afanasiev, A., Ganushkina, N. Y., Amariutei, O. A., Boscher, D., Sicard, A., et al. (2013). Forecasting the earth's radiation belts and modelling solar energetic particle events: Recent results from spacecast. *Journal of Space Weather and Space Climate*, 3:A20.

Horne, R. B., Meredith, N. P., Thorne, R. M., Heynderickx, D., Iles, R. H., and Anderson, R. R. (2003). Evolution of energetic electron pitch angle distributions during storm time electron acceleration to megaelectronvolt energies. *Journal of Geophysical Research: Space Physics*, 108(A1).

Horne, R. B., Thorne, R. M., Shprits, Y. Y., Meredith, N. P., Glauert, S. A., Smith, A. J., Kanekal, S. G., Baker, D. N., Engebretson, M. J., Posch, J. L., et al. (2005). Wave acceleration of electrons in the van allen radiation belts. *Nature*, 437(7056):227–230.

Jacobs, J., Kato, Y., Matsushita, S., and Troitskaya, V. (1964). Classification of geomagnetic micropulsations. *Journal of Geophysical Research*, 69(1):180–181.

Jordanova, V., Albert, J., and Miyoshi, Y. (2008). Relativistic electron precipitation by emic waves from self-consistent global simulations. *Journal of Geophysical Research: Space Physics*, 113(A3).

Jordanova, V. and Miyoshi, Y. (2005). Relativistic model of ring current and radiation belt ions and electrons: Initial results. *Geophysical research letters*, 32(14).

Kennel, C. and Engelmann, F. (1966). Velocity space diffusion from weak plasma turbulence in a magnetic field. *The Physics of Fluids*, 9(12):2377–2388.

Lanzerotti, L. J. (2001). Space weather effects on technologies. *Space weather*, pages 11–22.

Lenchek, A., Singer, S., and Wentworth, R. (1961). Geomagnetically trapped electrons from cosmic ray albedo neutrons. *Journal of Geophysical Research*, 66(12):4027–4046.

Lerche, I. (1968). Quasilinear theory of resonant diffusion in a magneto-active, relativistic plasma. *The Physics of Fluids*, 11(8):1720–1727.

Li, W., Shprits, Y., and Thorne, R. (2007). Dynamic evolution of energetic outer zone electrons due to wave-particle interactions during storms. *Journal of Geophysical Research: Space Physics*, 112(A10).

Li, W., Thorne, R., Bortnik, J., Nishimura, Y., Angelopoulos, V., Chen, L., McFadden, J., and Bonnell, J. (2010). Global distributions of suprathermal electrons observed on themis and potential mechanisms for access into the plasmasphere. *Journal of Geophysical Research: Space Physics*, 115(A12).

Li, X., Baker, D., Temerin, M., Reeves, G., and Belian, R. (1998). Simulation of dispersionless injections and drift echoes of energetic electrons associated with substorms. *Geophysical research letters*, 25(20):3763–3766.

Liemohn, M. W. and Brandt, P. C. (2005). Small-scale structure in the stormtime ring current. *Inner Magnetosphere Interactions: New Perspectives from Imaging*, pages 167–177.

Liu, S., Chen, M., Lyons, L., Korth, H., Albert, J., Roeder, J., Anderson, P., and Thomsen, M. (2003). Contribution of convective transport to stormtime ring current electron injection. *Journal of Geophysical Research: Space Physics*, 108(A10).

Lyons, L. (1984). Electron energization in the geomagnetic tail current sheet. *Journal of Geophysical Research: Space Physics*, 89(A7):5479–5487.

Lyons, L., Thorne, R., and Kennel, C. (1971). Electron pitch-angle diffusion driven by oblique whistler-mode turbulence. *Journal of Plasma Physics*, 6(3):589–606.

Lyons, L. R. and Thorne (1973). Equilibrium structure of radiation belt electrons. *Journal of Geophysical Research*, 78(13):2142–2149.

Lyons, L. R., Thorne, R. M., and Kennel, C. F. (1972). Pitch-angle diffusion of radiation belt electrons within the plasmasphere. *Journal of Geophysical Research*, 77(19):3455–3474.

Meredith, N. P., Horne, R. B., Glauert, S. A., and Anderson, R. R. (2007). Slot region electron loss timescales due to plasmaspheric hiss and lightning-generated whistlers. *Journal of Geophysical Research: Space Physics*, 112(A8).

Millan, R. and Baker, D. (2012). Acceleration of particles to high energies in earth's radiation belts. *Space Science Reviews*, 173(1-4):103–131.

Miyoshi, Y., Jordanova, V., Morioka, A., Thomsen, M., Reeves, G., Evans, D., and Green, J. (2006). Observations and modeling of energetic electron dynamics during the october 2001 storm. *Journal of Geophysical Research: Space Physics*, 111(A11).

Miyoshi, Y., Morioka, A., Misawa, H., Obara, T., Nagai, T., and Kasahara, Y. (2003). Rebuilding process of the outer radiation belt during the 3 november 1993 magnetic storm: Noaa and exos-d observations. *Journal of Geophysical Research: Space Physics*, 108(A1).

Ni, B., Thorne, R. M., Shprits, Y. Y., and Bortnik, J. (2008). Resonant scattering of plasma sheet electrons by whistler-mode chorus: Contribution to diffuse auroral precipitation. *Geophysical Research Letters*, 35(11).

O'Brien, T. (2014). Breaking all the invariants: Anomalous electron radiation belt diffusion by pitch angle scattering in the presence of split magnetic drift shells. *Geophysical Research Letters*, 41(2):216–222.

Odenwald, S., Green, J., and Taylor, W. (2006). Forecasting the impact of an 1859-calibre superstorm on satellite resources. *Advances in Space Research*, 38(2):280–297.

Ohtani, S.-i. (1998). Earthward expansion of tail current disruption: Dual-satellite study. *Journal of Geophysical Research: Space Physics*, 103(A4):6815–6825.

Orlova, K. and Shprits, Y. (2014). Model of lifetimes of the outer radiation belt electrons in a realistic magnetic field using realistic chorus wave parameters. *Journal of Geophysical Research: Space Physics*, 119(2):770–780.

Orlova, K., Shprits, Y., and Spasojevic, M. (2016). New global loss model of energetic and relativistic electrons based on van allen probes measurements. *Journal of Geophysical Research: Space Physics*, 121(2):1308–1314.

Orlova, K., Spasojevic, M., and Shprits, Y. (2014). Activity-dependent global model of electron loss inside the plasmasphere. *Geophysical Research Letters*, 41(11):3744–3751.

Reeves, G., Baker, D., Belian, R., Blake, J., Cayton, T., Fennell, J., Friedel, R., Meier, M., Selesnick, R., and Spence, H. E. (1998). The global response of relativistic radiation belt electrons to the january 1997 magnetic cloud. *Geophysical research letters*, 25(17):3265–3268.

Reeves, G., Henderson, M., McLachlan, P., Belian, R., Friedel, R., and Korth, A. (1996). Radial propagation of substorm injections. In *International conference on substorms*, volume 389, page 579.

Reeves, G., McAdams, K., Friedel, R., and O'Brien, T. (2003). Acceleration and loss of relativistic electrons during geomagnetic storms. *Geophysical Research Letters*, 30(10).

Rodriguez, J. (2014). Goes epead science-quality electron fluxes algorithm theoretical basis document. *NOAA Nat. Geophys. Data Center.*

Rothwell, P. and McIlwain, C. E. (1960). Magnetic storms and the van allen radiation belts—observations from satellite 1958ε (explorer iv). *Journal of Geophysical Research*, 65(3):799–806.

Russell, C. and Thorne, R. (1970). On the structure of the inner magnetosphere. In *Cosmic Electrodynamics*, volume 1, pages 67–89.

Sarris, T. E., Li, X., Tsaggas, N., and Paschalidis, N. (2002). Modeling energetic particle injections in dynamic pulse fields with varying propagation speeds. *Journal of Geophysical Research: Space Physics*, 107(A3).

Schulz, M. and Lanzerotti, L. J. (1974). Particle diffusion in the radiation belts. *Physics and Chemistry in Space*, 7.

Sergeev, V., Shukhtina, M., Rasinkangas, R., Korth, A., Reeves, G., Singer, H., Thomsen, M., and Vagina, L. (1998). Event study of deep energetic particle injections during substorm. *Journal of Geophysical Research: Space Physics*, 103(A5):9217–9234.

Sergeev, V. and Tsyganenko, N. (1982). Energetic particle losses and trapping boundaries as deduced from calculations with a realistic magnetic field model. *Planetary and Space Science*, 30(10):999–1006.

Sheeley, B., Moldwin, M., Rassoul, H., and Anderson, R. (2001). An empirical plasmasphere and trough density model: Crres observations. *Journal of Geophysical Research: Space Physics*, 106(A11):25631–25641.

Shprits, Y. and Thorne, R. (2004). Time dependent radial diffusion modeling of relativistic electrons with realistic loss rates. *Geophysical research letters*, 31(8).

Shprits, Y., Thorne, R., Friedel, R., Reeves, G., Fennell, J., Baker, D., and Kanekal, S. (2006). Outward radial diffusion driven by losses at magnetopause. *Journal of Geophysical Research: Space Physics*, 111(A11).

Shprits, Y., Thorne, R., Reeves, G., and Friedel, R. (2005). Radial diffusion modeling with empirical lifetimes: Comparison with crres observations. In *Annales Geophysicae*, volume 23, pages 1467–1471.

Shprits, Y. Y., Chen, L., and Thorne, R. M. (2009a). Simulations of pitch angle scattering of relativistic electrons with mlt-dependent diffusion coefficients. *Journal of Geophysical Research: Space Physics*, 114(A3).

Shprits, Y. Y., Elkington, S. R., Meredith, N. P., and Subbotin, D. A. (2008a). Review of modeling of losses and sources of relativistic electrons in the outer radiation belt i: Radial transport. *Journal of Atmospheric and Solar-Terrestrial Physics*, 70(14):1679–1693.

Shprits, Y. Y., Meredith, N. P., and Thorne, R. M. (2007). Parameterization of radiation belt electron loss timescales due to interactions with chorus waves. *Geophysical research letters*, 34(11).

Shprits, Y. Y. and Ni, B. (2009). Dependence of the quasi-linear scattering rates on the wave normal distribution of chorus waves. *Journal of Geophysical Research: Space Physics*, 114(A11).

Shprits, Y. Y., Subbotin, D., and Ni, B. (2009b). Evolution of electron fluxes in the outer radiation belt computed with the verb code. *Journal of Geophysical Research: Space Physics*, 114(A11).

Shprits, Y. Y., Subbotin, D. A., Meredith, N. P., and Elkington, S. R. (2008b). Review of modeling of losses and sources of relativistic electrons in the outer radiation belt ii: Local acceleration and loss. *Journal of atmospheric and solar-terrestrial physics*, 70(14):1694–1713.

Starks, M., Quinn, R., Ginet, G., Albert, J., Sales, G., Reinisch, B., and Song, P. (2008). Illumination of the plasmasphere by terrestrial very low frequency transmitters: Model validation. *Journal of Geophysical Research: Space Physics*, 113(A9).

Subbotin, D. and Shprits, Y. (2009). Three-dimensional modeling of the radiation belts using the versatile electron radiation belt (verb) code. *Space Weather*, 7(10).

Subbotin, D., Shprits, Y., Gkioulidou, M., Lyons, L., Ni, B., Merkin, V., Toffoletto, F., Thorne, R., Horne, R. B., and Hudson, M. (2011a). Simulation of the acceleration of relativistic electrons in the inner magnetosphere using rcm-verb coupled codes. *Journal of Geophysical Research: Space Physics*, 116(A8).

Subbotin, D., Shprits, Y., and Ni, B. (2010). Three-dimensional verb radiation belt simulations including mixed diffusion. *Journal of Geophysical Research: Space Physics*, 115(A3).

Subbotin, D., Shprits, Y., and Ni, B. (2011b). Long-term radiation belt simulation with the verb 3-d code: Comparison with crres observations. *Journal of Geophysical Research: Space Physics*, 116(A12).

Thorne, R., Li, W., Ni, B., Ma, Q., Bortnik, J., Baker, D., Spence, H. E., Reeves, G., Henderson, M., Kletzing, C., et al. (2013). Evolution and slow decay of an unusual narrow ring of relativistic electrons near l˜ 3.2 following the september 2012 magnetic storm. *Geophysical Research Letters*, 40(14):3507–3511.

Tsyganenko, N. A. (1995). Modeling the earth's magnetospheric magnetic field confined within a realistic magnetopause. *Journal of Geophysical Research: Space Physics*, 100(A4):5599–5612.

Turner, D., Angelopoulos, V., Li, W., Bortnik, J., Ni, B., Ma, Q., Thorne, R., Morley, S., Henderson, M., Reeves, G., et al. (2014). Competing source and loss mechanisms due to wave-particle interactions in earth's outer radiation belt during the 30 september to 3 october 2012 geomagnetic storm. *Journal of Geophysical Research: Space Physics*, 119(3):1960–1979.

Van Allen, J. A. (1959). Radiation belts around the earth. *Scientific American*, 200(3):39–47.

Van Allen, J. A. and Frank, L. A. (1959). Radiation around the earth to a radial distance of 107,400 km. *Nature*, 183(4659):430–434.

Varotsou, A., Boscher, D., Bourdarie, S., Horne, R. B., Glauert, S. A., and Meredith, N. P. (2005). Simulation of the outer radiation belt electrons near geosynchronous orbit including both radial diffusion and resonant interaction with whistler-mode chorus waves. *Geophysical research letters*, 32(19).

Varotsou, A., Boscher, D., Bourdarie, S., Horne, R. B., Meredith, N. P., Glauert, S. A., and Friedel, R. H. (2008). Three-dimensional test simulations of the outer radiation belt electron dynamics including electron-chorus resonant interactions. *Journal of Geophysical Research: Space Physics*, 113(A12).

Vernov, S. and Chudakov, A. (1960). Investigation of radiation in outer space. In *International Cosmic Ray Conference*, volume 3, page 19.

Walt, M. (1994). Introduction to geomagnetically trapped radiation. *Camb. Atmos. Space Sci. Ser., Vol. 10,*, 10.

Xiao, F., Su, Z., Zheng, H., and Wang, S. (2010). Three-dimensional simulations of outer radiation belt electron dynamics including cross-diffusion terms. *Journal of Geophysical Research: Space Physics*, 115(A5).